Intracrustal partial melting of garnet amphibolite from southwestern Sweden - a possible analogue for TTG formation

Ylva Magnell

Dissertations in Geology at Lund University,
Bachelor's thesis, no 736
(15 hp/ECTS credits)

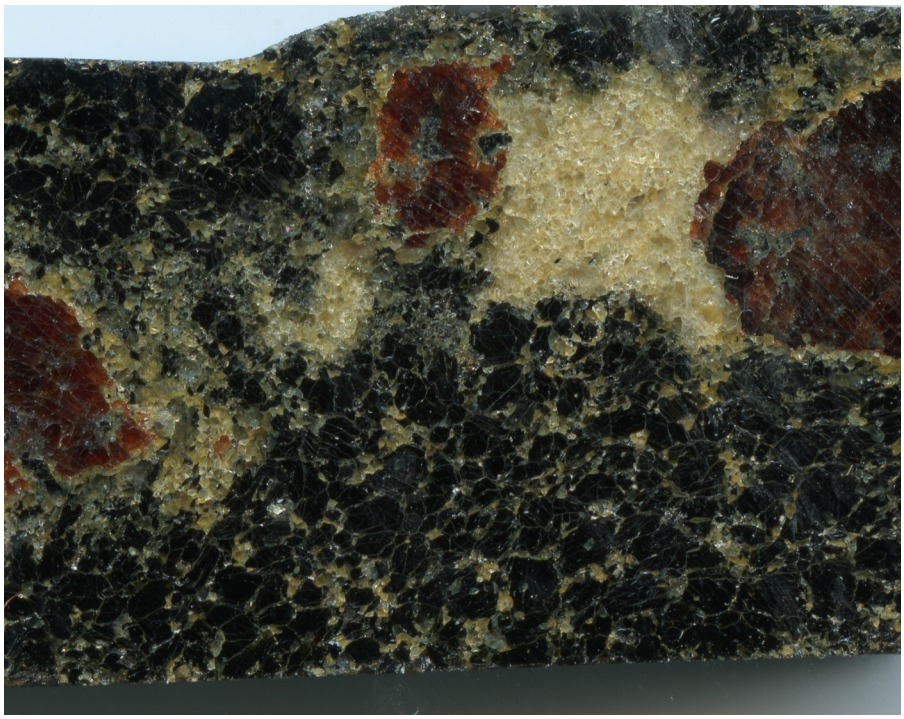

Department of Earth and Environmental Sciences
Lund University
2026

Intracrustal partial melting of garnet amphibolite from southwestern Sweden - a possible analogue for TTG formation

Bachelor's thesis

Ylva Magnell

Department of Earth and Environmental Sciences
Lund University
2026

Contents

Cover Picture: Polished 45 x 25 mm section of garnet amphibolite with melt pockets from Varberg, Sweden. Photo: Anders Scherstén.

Intracrustal partial melting of garnet amphibolite from southwestern Sweden - a possible analogue for TTG formation

YLVA MAGNELL

Magnell, Y., 2026: Intracrustal partial melting of garnet amphibolite from southwestern Sweden - a possible analogue for TTG formation. *Dissertations in Geology at Lund University*, No. 736, 36 pp. 15 hp (15 ECTS credits).

Abstract: The Archean crust is the oldest preserved continental crust on Earth, and it is largely made up of the rock suite tonalite-trondhjemite-granodiorite (TTG). Quartz and plagioclase are the dominating minerals of TTG rocks, that are characterized by a high SiO_2, Na_2O, and a low K_2O. TTG rarely form today which have led to an uncertainty around their origin, but they are believed to be generated through partial melting of meta-basalts. A garnet amphibolite containing quartz and plagioclase rich areas that are thought to be the result of partial melting, were analyzed in this study to get a better understanding of TTG formation. The garnet amphibolite outcrop is located in the Eastern Segment, which were affected by the Sveconorwegian orogeny through underthrusting. Analyses of the quartz-plagioclase areas show a high SiO_2 (>70 wt. %), high Na_2O (2.0-6.0 wt. %), and low K_2O (< 1.0 wt. %), which are comparable with TTG composition. The amphibolite matrix is largely dominated by hornblende and plagioclase, but finer grained clinopyroxene bearing areas are also observed. The distribution of the quartz-plagioclase areas and variations in the matrix corroborates the assumption that the rock has been through partial melting. The presence of garnet, absence of epidote and the clinopyroxene bearing areas in the matrix, indicates temperatures above 850 °C and pressures over 10 kbar. Based on conditions that affected the area during the Sveconorwegian orogeny, the results suggests that TTG-melts could be generated through intracrustal partial melting of garnet amphibolite and without the need of an extensive subduction zone.

Keywords: TTG, tonalite-trondhjemite-granodiorite, garnet amphibolite, partial melt, geochemistry, Sveconorwegian orogeny, Eastern Segment.

Supervisor(s): Anders Scherstén, Chris Hawkesworth, Tomas Næraa, Andreas Petersson

Subject: Bedrock Geology

Ylva Magnell, Department of Earth and Environmental Sciences, Lund University, Sölvegatan 12, SE-223 62 Lund, Sweden. E-mail: yl6003ma-s@student.lu.se

Infrakrustal partiell uppsmältning av granatamfibolit från sydvästra Sverige – en möjlig analog för TTG formation

YLVA MAGNELL

Magnell, Y., 2026: Infrakrustal partiell uppsmältning av granatamfibolit från sydvästra Sverige – en möjlig analog för TTG formation. *Examensarbeten i geologi vid Lunds universitet*, Nr. 736, 36 sid. 15 hp.

Sammanfattning: Den arkeiska jordskorpan är den äldsta bevarade kontinentala jordskorpan på jorden och den består till stor del av bergartssviten tonalit-trondhjemit-granodiorit (TTG). Kvarts och plagioklas är de dominerande mineralen i TTG bergarter, som karakteriseras av hög SiO_2, Na_2O och låg K_2O. TTG bildas sällan idag vilket har lett till en osäkerhet runt deras ursprung, men de tros vara bildade genom partiell uppsmältning av meta-basalter. En granatamfibolit innehållande kvarts och plagioklas rika områden som förmodas vara resultatet av partiell uppsmältning, analyserades i denna studie för att få en bättre förståelse av TTG bildning. Granatamfibolit hällen är belägen i Östra Segmentet som påverkades av den Svekonorvegiska orogensen genom underskjutning. Analyser av kvarts-plagioklas områden visar hög SiO_2 (>70 wt. %), hög Na_2O (2.0-6.0 wt. %), och låg K_2O (<1.0 wt. %), vilka är jämförbara med TTG sammansättning. Amfibolit matrix är dominerad av hornblände och plagioklas, men finkorniga klinopyroxen bärande områden observeras även. Utbredningen av kvarts-plagioklas områdena och variationer i matrix stärker antagandet att bergarten har genomgått partiell uppsmältning. Förekomsten av granat, frånvaron av epidot och klinopyroxen bärande områden i matrix, indikerar temperaturer över 850 °C och tryck över 10 kbar. Baserat på förhållanden som området utsattes för under den Svekonorvegiska orogenesen, föreslår resultatet att TTG-smältor kan bildas genom infrakrustal partiell uppsmältning av granatamfibolit utan att det behövs en omfattande subduktionszon.

Nyckelord: TTG, tonalit-trondhjemit-granodiorit, granatamfibolit, partiell uppsmältning, geokemi, Svekonorvegiska orogenesen, Östra Segmentet.

Handledare: Anders Scherstén, Chris Hawkesworth, Tomas Næraa, Andreas Petersson

Ämnesinriktning: Berggrundsgeologi

Ylva Magnell, Miljö– och geovetenskapliga institutionen, Lunds universitet, Sölvegatan 12, 223 62 Lund, Sverige.
E-post: yl6003ma-s@student.lu.se

1 Introduction

The continental crust is the home of terrestrial habitats, and its formation has an import role in the evolution of the Earth. The oldest preserved continental crust found on Earth today formed during the Archean eon (4.0-2.5 Ga). This Archean crust is dominated by tonalite-trondhjemite-granodiorite (TTG), which are rocks composed of primarily quartz, oligoclase and biotite and characterized by high percentages of silica (SiO_2) and sodium (Na), and low amounts of potassium (K) (Moyen & Martin, 2012). This composition differs markedly form the K-rich, often granitic, crust of the Proterozoic and Phanerozoic (Moyen & Martin, 2012; Pourteau et al., 2020). The origin of TTG-rocks remains uncertain and how they formed in relation to tectonic settings, source magma and melting processes is still debated. There is general agreement that the geochemical signatures of TTG rocks are best explained through partial melting of meta-basalts, which is corroborated by melting experiments (Moyen & Martin, 2012). Different tectonic settings have been proposed for the formation of TTGs, such as subduction zones or intraplate environments.

This study is based on a garnet amphibolite from Varberg, which is located within the high-grade gneiss terrain of the Eastern Segment in southwestern Sweden (Bingen et al., 2021). The sampled rock appears to have been through partial melting, and I explore the extent to which this process is analogous to TTG-melt formation. The purpose of this thesis is to study the assumed partial melt and unmelted residue, with the aim to increase the understanding of how TTG-melts can form. The material is unique since the melt coexists with the residual material. This would enable an investigation of geological conditions and how they affect element fractionation during melting. To answer the purpose the following research questions will be targeted:

Can the presence of quartz-plagioclase rich rock patches be explained through partial melting of the garnet amphibolite?

What do the petrography and geochemistry of the melt and unmelted residue imply of the conditions during melting?

Is the composition of the partial melt similar to TTG-melts?

Under what conditions can TTG-melts form?

Petrographic and geochemical analyses of major elements was carried out to target these questions that will be able to provide contributions in the constraint of TTG-formation and give insight in the evolution of the early continental crust.

2 Background

2.1 Crustal evolution

The Earth has cooled progressively since its formation and this affects the characteristics of plate tectonics through time, as a hotter mantle with a lower viscosity and a higher melt production might limit plate movements (Davies, 1992; van Hunen & van den Berg, 2008). Rocks from the Archean eon (4.0-2.5 Ga) has an important role in the study of the early evolution of the continental crust, as they make up the oldest silicate crust that can be studied on Earth today (Frost & Mueller, 2024). In the Archean, the temperature of the Earth was higher which would have an effect on crustal composition and thickness (Sizova et al., 2015). The temperature of the early Archean upper mantle is believed to have reached around 1600 °C compared to the average present-day temperature of 1280-1400 °C (Sizova et al., 2015 and references therein). During the Archean, the Earth also had a higher production of radiogenic heat, considered to possibly have been three times higher than the present (Davies, 1992). With regards to the progressive cooling of the Earth, the higher temperature of the Archean mantle is an important difference from modern conditions which makes an understanding of the crustal formation in the Archean more challenging (Sizova et al., 2015).

2.2 Tonalite-trondhjemite-granodiorite rocks

The main rock assemblages that make up the Archean cratons are grey gneisses and greenstone belts (Frost & Mueller, 2024). The tonalite-trondhjemite-granodiorite (TTG) suite is dominating the grey gneiss complexes (Moyen, 2011). TTGs are not commonly formed today and they therefore make up a key component for understanding the evolution of the Earth's Archean continental crust (Moyen, 2011).

Quartz, oligoclase (plagioclase with An_{10}-An_{30}) and biotite are the dominating minerals in TTGs (Moyen & Martin, 2012). TTGs are characterized by high amounts of SiO_2 (>64 wt.%) and Na_2O (3.0-7.0 wt.%) (Moyen & Martin, 2012). They have low amounts of K_2O, in contrast to the more K-rich crustal granitoids of the Proterozoic and Phanerozoic (Moyen & Martin, 2012; Pourteau et al., 2020; Fig. 1). TTGs are commonly depleted in ferromagnesian elements ($\Sigma_{FeO+MnO+MgO}$ < 4 wt. %), have low average Mg# ~ 0.43 and a high alumina content (Al_2O_3 > 15 % at 70 % SiO_2) (Barker, 1979; Moyen & Martin, 2012). Fractionated rare earth elements (REE) and depletion of heavy rare earth elements (HREE) is typical for TTGs (Moyen, 2011). Although these characteristics are commonly used to define TTGs, differences in the geochemistry are seen, which has led to various divisions of the suite. There are three main groups that correlate with different melting pressures (Moyen, 2011). Al_2O_3-, Na_2O- and Sr-concentrations are elevated in the high-pressure group, intermediate in the medium-pressure group and lower in the low-pressure group (Moyen, 2011). The high-pressure group also shows lower concentrations of HREE, Nb and Ta, with the low-pressure group showing the opposite trends (Moyen, 2011).

Through geochemical analyses of TTGs and melting experiments, they appear to have been derived from partial melting of meta-basalts (Barker et al., 1981; Moyen & Martin, 2012; Zhang et al., 2013). The geochemical character of TTGs have also been used to define possible scenarios for their formation (Moyen & Martin, 2012). Various melting experiments of amphibolites with different starting mineralogy

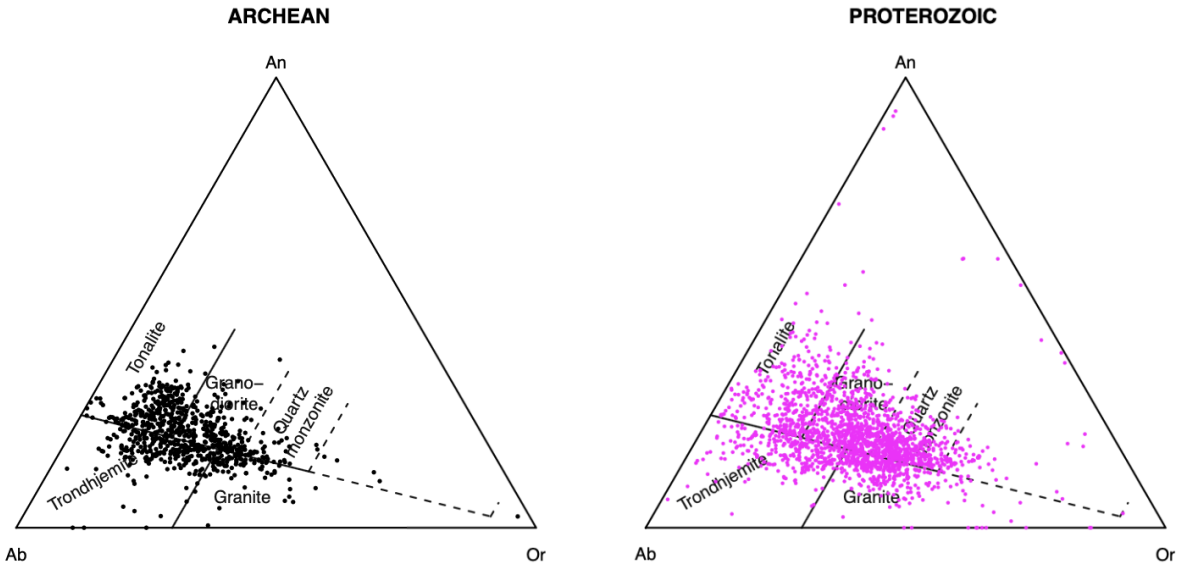

Fig. 1. CIPW-normative feldspar composition diagram of Archean TTGs (black dots) and Proterozoic granitoids (pink dots). Plot of Archean TTGs is composed of 788 data samples and plot of Proterozoic granitoids is composed of 1962 data samples (Data were downloaded from the GEOROC database (https://georoc.eu/) on 1-2 April 2026, using the following parameters: Petrography And Samples = 2. Plutonic Rocks; and rock names: = trondhjemit(e/ic), = granodiorit(e/ic), = tonalit(e/ic)). Data was later filtered on geological age into Archean and Proterozoic.

indicate the formation of TTGs at pressures above 15 kbar and 900°C to 1100 °C (Moyen & Stevens, 2006). These conditions imply a geothermal gradient of ~20 ° C/km, which is thought to be possible in a subduction setting with higher heat than today (Moyen & Stevens, 2006). However, the generation of TTGs through melting of meta-basalts could occur in various tectonic environments. Melting at the base of a hydrated thick basaltic crust has also been argued to be a possible setting for the formation of TTGs (Smithies, 2000; Willbold et al., 2009; Zhang et al., 2013; Johnson et al., 2017; Smit et al., 2024).

2.3 Regional geology

2.3.1 The Sveconorwegian orogeny

The southwestern margin of Fennoscandia is part of the Sveconorwegian orogen (Bingen et al., 2008). The continental crust formed through magmatism and accretion in orogenies that extended between 1910 and 1380 Ma (Bingen et al., 2021). During the Sveconorwegian orogeny (1140 to 920 Ma) the crust was reworked by metamorphism, deformation and magmatism, and most geodynamic models infer a collision between two continental plates (Bingen et al., 2008). Shear zones divide the Sveconorwegian belt into lithotectonic units which include the Eastern Segment, that is interpreted to be parautochthonous, and the accreted Telemarkia-, Bamble-, Kongsberg- and Idefjorden terranes (Bingen et al., 2008; Fig. 2).

2.3.2 The Eastern Segment

The Eastern Segment is located furthest east in the Sveconorwegian orogen and borders to the Fennoscandia Foreland in the east and to the Mylonite Zone that separates it from the Idefjorden Terrane in the west (Fig. 2). The rocks of the Eastern Segment are dominated by orthogneisses that crystallized during a period between 1900 and 1660 Ma, but with a volume peak 1710-1660 Ma (Bingen et al., 2021). Crust in the southern part of the Eastern Segment was reworked during the Hallandian orogeny around 1465 to 1385 Ma (Bingen et al., 2021). The Eastern Segment was affected by the Sveconorwegian orogeny from 1000 Ma, and between 1000 and 980 Ma the eastern part of the collision zone experienced high grade metamorphism through underthrusting (Bingen et al., 2021). Eclogite facies has been recorded in the Eastern Segment, and dating of eclogite metamorphism has yielded the maximum age of 988 ± 7 Ma (Möller et al., 2015). Exhumation of the Eastern Segment occurred between 980 to 940 Ma and was followed by the collapse of the orogenic plateau after 930 Ma (Bingen et al., 2021). High grade metamorphism in the Eastern Segment occurred at 980-970 Ma (Bingen et al., 2008; Möller & Andersson, 2018). This event includes the alteration of mafic rocks through recrystallization that is associated with deformation and the presence of hydrous fluids (Möller & Andersson, 2018). Mafic rocks of the Eastern Segment include predominantly amphibolite, mafic granulite, and rare eclogite (Möller et al., 2015). Metamorphism of mafic rocks in the southern part of the Eastern Segment occurred in amphibolite to granulite facies at temperatures between 680 to 800 °C and pressures of 0.85-1.17 GPa (Wang & Lindh, 1996).

Varberg is located near the western margin of the Eastern Segment, directly south of the border to the Idefjorden terrane (Fig. 2). The Varberg area is primarily composed of high-grade metamorphic gneissic granitic rocks and charnockites (Johansson & Kullerud, 1993). These rocks are accompanied by altered mafic dykes and bodies, with mineral assemblages in the amphibolite to granulite facies (Johansson & Kullerud, 1993). Dating of a mafic granulite from the Varberg region has yielded the age of 881 ± 4 Ma (Johansson & Kullerud, 1993).

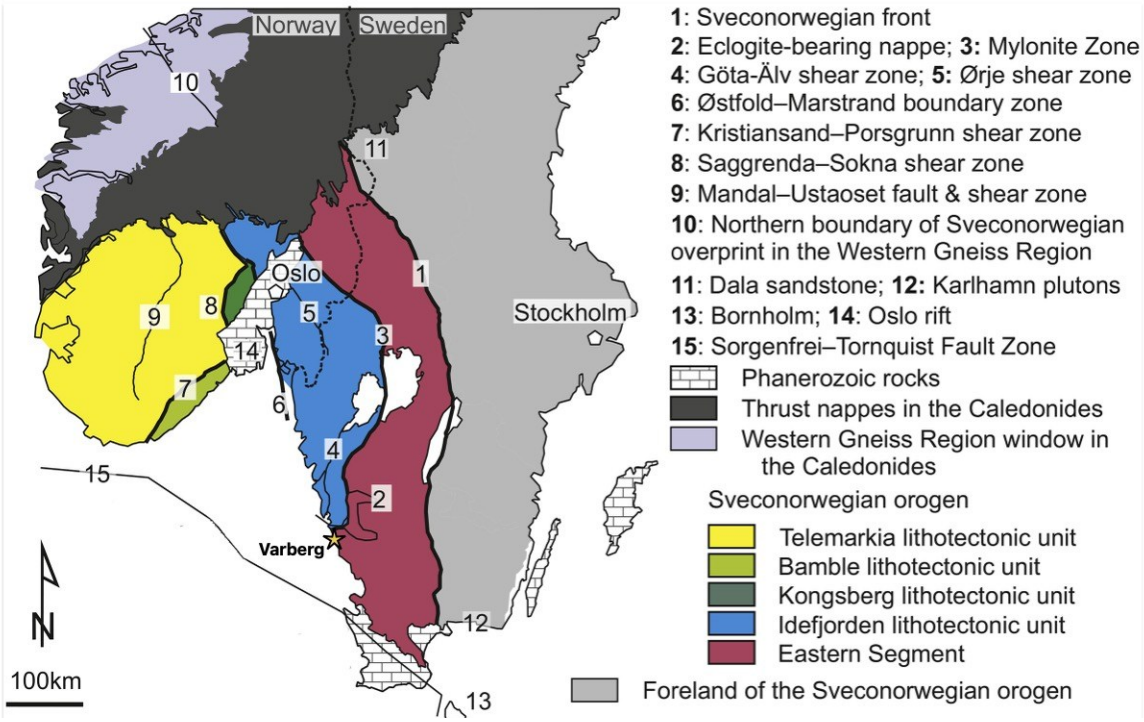

Fig. 2. Regional division of the Sveconorwegian belt. The sample locality Varberg is marked out. Modified after Bingen et al., 2021.

3 Samples and methods

3.1 Samples

Two samples from Getterön, west of Varberg, from the collection at the Department of Earth and Environmental Sciences at Lund University, were examined. The samples represent a garnet amphibolite and a melt accumulation vein in amphibolite, both collected as loose boulders at the Sillhallsvik on Getterön in Varberg (Fig. 3). The samples were found in direct relation with an outcrop that expose garnet amphibolite of similar composition and are assumed to be representative of the outcrop rocks and general processes that affected the region.

3.2 Section preparation

Seven slabs of the rock samples, approximately 1-2 cm in thickness, were sawed from the boulders. The slabs were scanned on a flatbed scanner to document internal textures and to select 45 x 25 mm areas based on amount of melt concentrations (see Appendix I for

Fig. 3. Map over Getterön and Varberg. Sample locality is marked out with coordinates. (Retrieved May 4, 2026 from Google Earth Pro v7.3.7.).

placement). 45 x 25 mm sections were sawed out of which the nine foremost were selected for polishing. The polishing was carried out on a polishing disc in six steps. A mixture of Silicon Carbide Powder, glycerol and water were used for the first steps, starting with 220 grith followed by 1000 grith. The succeeding polishing was carried on 9 µm, 6 µm, 3 µm and 1 µm polishing discs with diamond paste.

3.3 Scanning electron microscopy – energy dispersive spectroscopy (SEM-EDS)

The selected sections were carbon coated with a 12 nm thick carbon layer using an Agar Auto Carbon Coater to prevent charging during SEM work. Analyses of four sections was done in a TESCAN Mira3 Field Emission Scanning Electron Microscope at the Department of Earth and Environmental Sciences at Lund University. Three sections (2A (1/3), 3 (2/3) and 4 (3/5)) from the garnet amphibolite sample were analyzed. Section 2A (1/3) and 4 (3/5) were chosen since they have larger domains composed of quartz and plagioclase (qz-plag) that is assumed to be representative of the qz-plag areas throughout the rock sample (these domains are of interest since they are thought to possibly be the result of partial melting). Section 3 (2/3) was chosen since it contained a domain where the matrix exhibited a compositional variation. Section T1 (1/2) was chosen to be representative for the larger melt accumulation vein sample. The analyses were done with the acceleration voltage at 15.00 kV and beam intensity of 16.00 nA.

SEM uses an electron beam onto a sample, causing interactions that are used to produce an image (Korchinski et al., 2019). SEM coupled with backscatter electron imaging (BSE) was used to visualize the distribution of minerals. BSE implies elastic interactions where some of the emitted electrons backscatter from the surface of the sample (Korchinski et al., 2019). The amount of backscattered electrons will depend on the size of the nucleus, where an increase in nucleus size increases the amount of backscattered electrons. This produces an image with lighter and darker fields representing different minerals. Chemical analyses were done with an energy dispersive spectroscopy (EDS) that is mounted in the SEM. EDS detects elements by a measurement of X-ray energy, produced by emitted electrons that transmit energy causing electrons on the targeted area to excite (Korchinski et al., 2019). Different elements will require a specific energy that is dependent on the electronic shells (K, L, M, etc.) (Korchinski et al., 2019), and this enables the detection of the elements.

Quantitative chemical analyses were done using Oxford Instrument's software AZtec, with a combination of mapping and point analyses. AZtec's factory standardisations database was used as standard for the quantitative analyses. The analyses were not calibrated against the cobalt standard that is normally used, due to the thickness of the sections and placement of the cobalt standard, which made the movement a high-risk to damage the detector. All results were normalized to 100% and reported as oxides. Previous work with this SEM setup indicates that molar proportions remain correct even if the data is normalized, and therefore the assumption is made that this is the case for these analyses too. Mapping was done to examine distribution of elements and possible zonation. Point analyses using the square function to mark out a 2000x2000 µm area was done to achieve an average "whole rock" element composition. Multiple square analyses of the qz-plag areas and matrix domains in the sections was carried out. The amount of square analyses in the different sections and domains varied depending on the size of the areas (see Appendix II & III for placement). Single point analyses were done to determine inclusions and mineral composition in the square areas. The data was processed in excel and GCDkit.

4 Results

4.1 Field observations

Variations in the garnet amphibolite outcrop at Sillhallsvik on Getterön, Varberg were observed. On the outer west edge of the outcrop, the amphibolite has a lineation defined by garnet and bands composed of quartz and plagioclase (Fig. 4). This area also held larger accumulations of quartz and plagioclase composition (Fig. 5). Approximately 10 meters further east into the bay the lineation became less pronounced, with euhedral garnet porphyroblasts distributed rather homogeneously in the matrix and smaller patches composed of quartz and plagioclase (Fig. 6).

Fig. 4. Garnet amphibolite with a lineation defined by garnet and bands composed of quartz and plagioclase, at Sillhallsvik on Getterön, Varberg.

Fig. 5. Garnet amphibolite with accumulations of quartz and plagioclase, at Sillhallsvik on Getterön, Varberg.

Fig. 6. Garnet amphibolite with patches of quartz and plagioclase, at Sillhallsvik on Getterön, Varberg.

4.2 Petrography

4.2.1 Garnet amphibolite (section 2A (1/3), 3 (2/3) and 4 (3/5))

This sample contains an amphibole bearing matrix with garnet porphyroblasts and light-colored areas of quartz and plagioclase (Fig. 7).

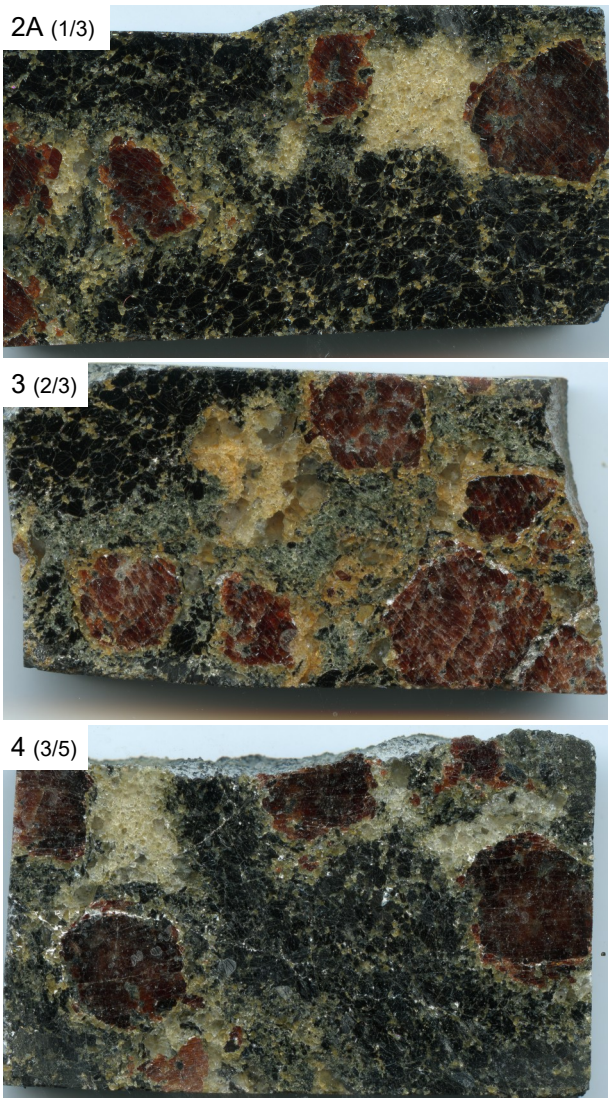

Fig. 7. Scanned 45 x 25 mm sections (2A (1/3), 3 (2/3) and 4 (3/5)) of the garnet amphibolite sample.

The matrix is dominated by amphibole, with smaller plagioclase crystals along grain boundaries. A textural and compositional variation is however observed in the matrix, with finer grained areas absent of macroscopic amphibole and with crystals identified as clinopyroxene. The fine-grained areas make up a large part of the matrix in section 3 (2/3), but smaller amounts of this texture can be observed in section 2 (1/3) and 4 (3/5) oriented near garnet porphyroblasts and the domains of quartz and plagioclase (Fig. 7). EDS-analyses of the finer grained area in section 3 (2/3) shows that it is composed of plagioclase, clinopyroxene and hornblende (Fig. 8). Inclusions in the matrix are dominated by ilmenite and apatite, but smaller amounts of pyrite, zircon and Fe-sulfides are also present.

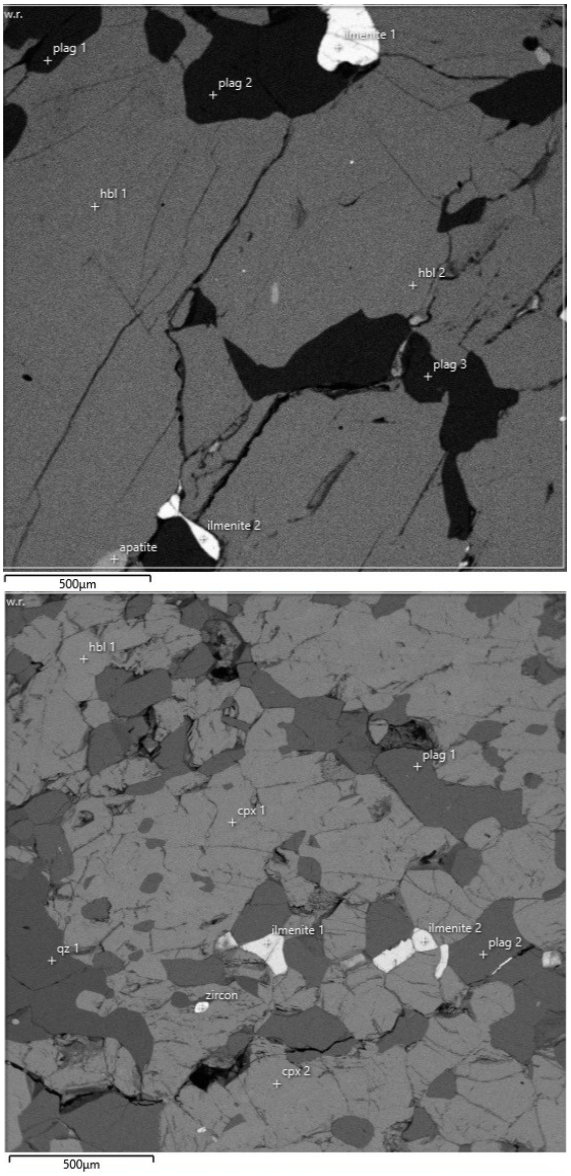

Fig. 8. SEM-images of compositional variation in the matrix of section 3 (2/3). Upper image show the area with macroscopic amphibole and plagioclase crystals. Lower image show the finer grained area that are composed of clinopyroxene, plagioclase and hornblende. Abbreviations: hbl: hornblende, plag: plagioclase, cpx: clinopyroxene, qz: quartz.

The light-colored areas are dominated by quartz and plagioclase and are mainly concentrated near garnet porphyroblasts (Fig. 7). In section 2A (1/3) and 4 (3/5) the domains have a similar size distribution between quartz and plagioclase crystals (Fig. 9), whereas the domain in section 3 (2/3) has larger quartz crystals that enclose smaller quartz and plagioclase crystals of similar size. Mineral inclusions appear in these domains and are dominated by ilmenite (Fig. 10). Inclusions of Ti-oxides, titanite, hornblende, apatite, clinopyroxene and zircon were also found (Fig. 11). A subarea in the larger qz-plag domain of section 2A (1/3) showed a plagioclase crystal that was partly enriched in potassium (K) (Fig. 12).

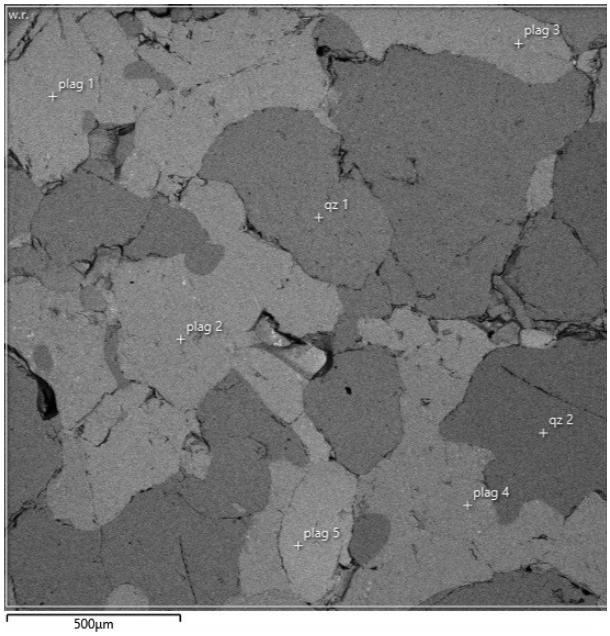

Fig. 9. SEM-image of qz-plag area in section 4 (3/5) which shows a similar crystal size between the minerals. Abbrevations: plag: plagioclase, qz: quartz.

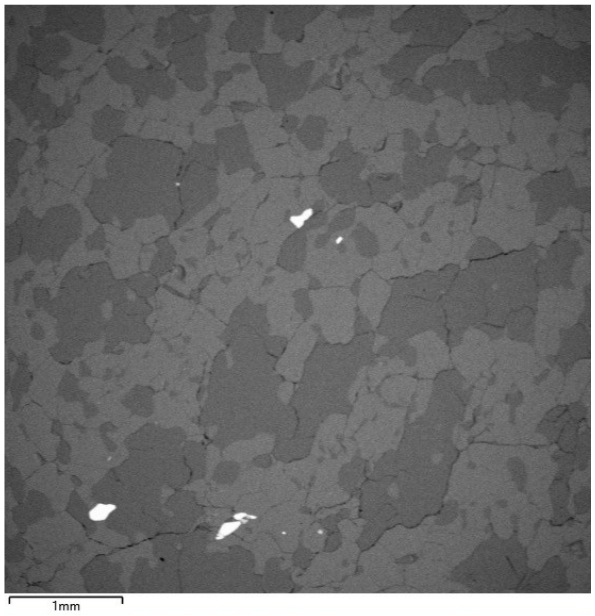

Fig. 10. SEM-image of qz-plag area in section 2A (1/3) with inclusions of ilmenite (white grains).

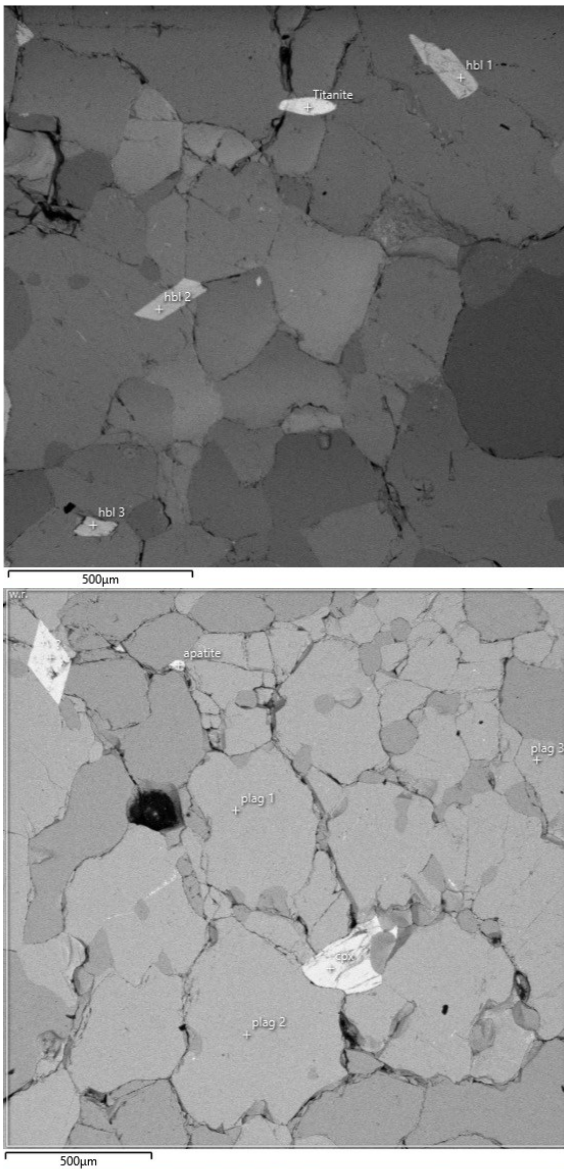

Fig. 11. SEM-images of qz-plag area with inclusions in section 4 (3/5). Abbreviations: hbl: hornblende, plag: plagioclase, cpx: clinopyroxene.

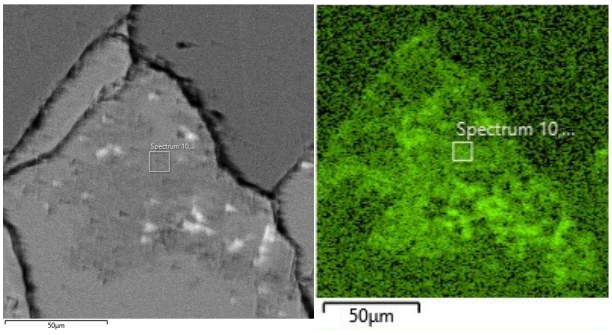

Fig. 12. SEM-image to the left of K-rich area in a plagioclase crystal in qz-plag area of section 2A (1/3). Image to the right shows elemental mapping of K in EDS-analysis of the area, showing an enrichment in K.

The garnet porphyroblasts make up around 25 volume percent and range in size from a few millimeters up to around 1 cm, with an average of approximately 5x5 mm (Fig. 7). In the polished sections, the garnet porphyroblasts appear as larger euhedral crystals and smaller unevenly shaped crystals. The garnet has inclusions of plagioclase, ilmenite and clinopyroxene that often were observed intergrown together in a symplectite texture (Fig. 13). Inclusions of quartz, hornblende, and rare orthopyroxene and titanite are also present.

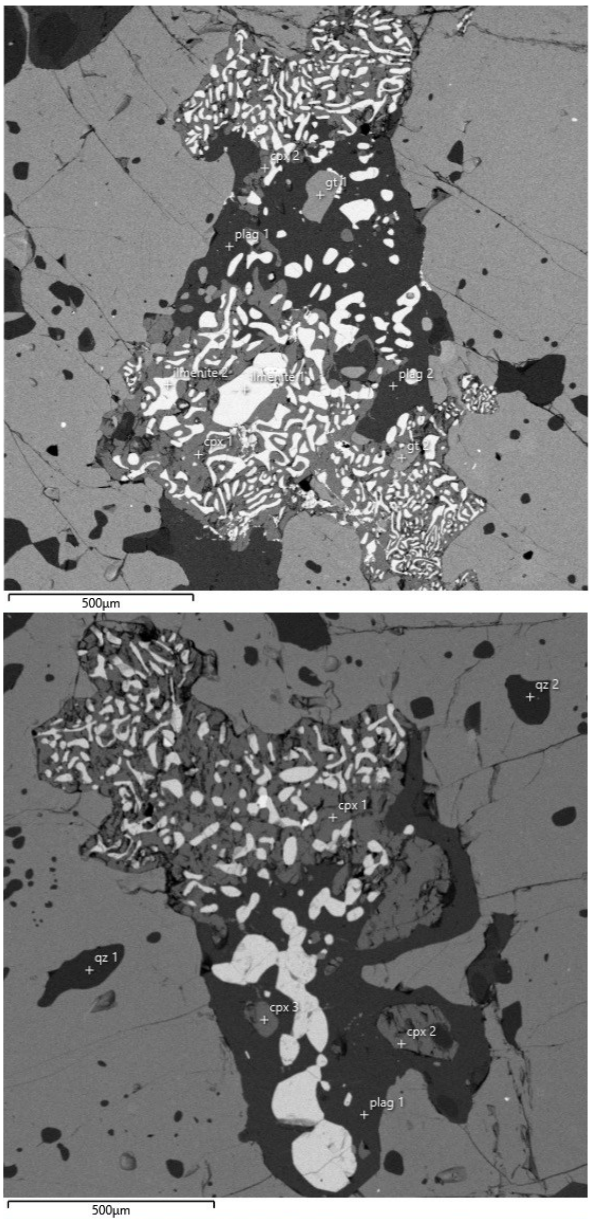

Fig. 13. SEM-images of garnet inclusions with clinopyroxene, plagioclase and ilmenite intergrown together (section 3 (2/3) and 4 (3/5)). Abbreviations: plag: plagioclase, cpx: clinopyroxene, gt: garnet, qz: quartz.

4.2.2 Melt accumulation vein (section T1 (1/2))

This sample is composed of a dark fine-grained matrix that is cut by a light-colored area of quartz and plagioclase crystals that is interpreted as a melt accumulation vein (Fig. 14). The matrix shows a compositional variation with finer grained domains, areas with macroscopic amphibole crystals and uneven sized garnet (Fig. 14 & 15). EDS-analyses of the finer grained matrix shows that it is composed of clinopyroxene, plagioclase and hornblende (Fig. 16).

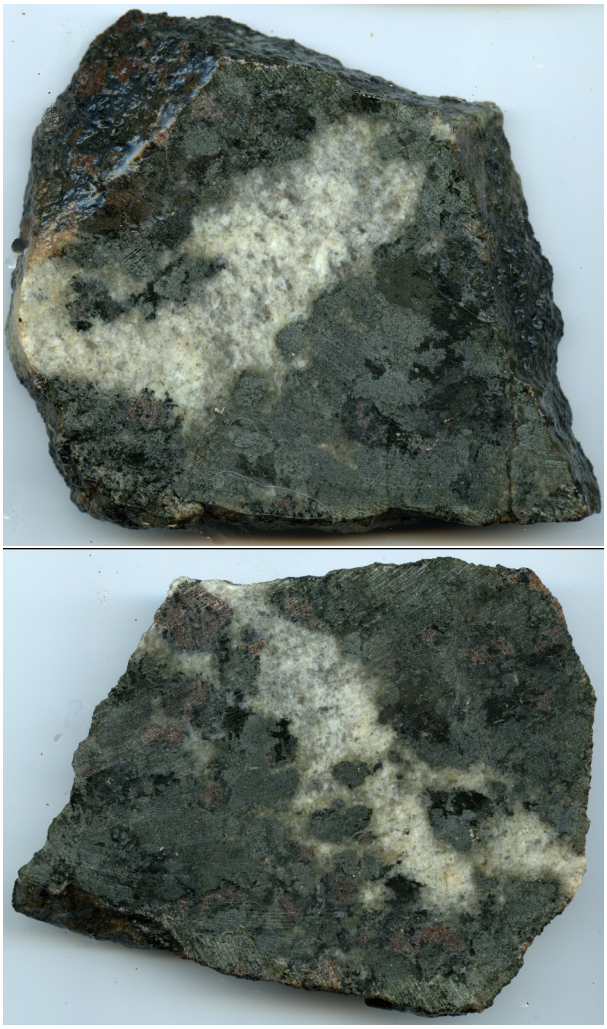

Fig. 14. Melt accumulation vein sample, slab T1.

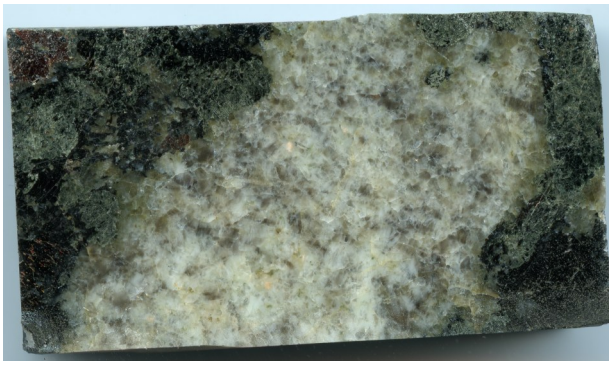

Fig. 15. Scanned 45 x 25 mm section T1 (1/2).

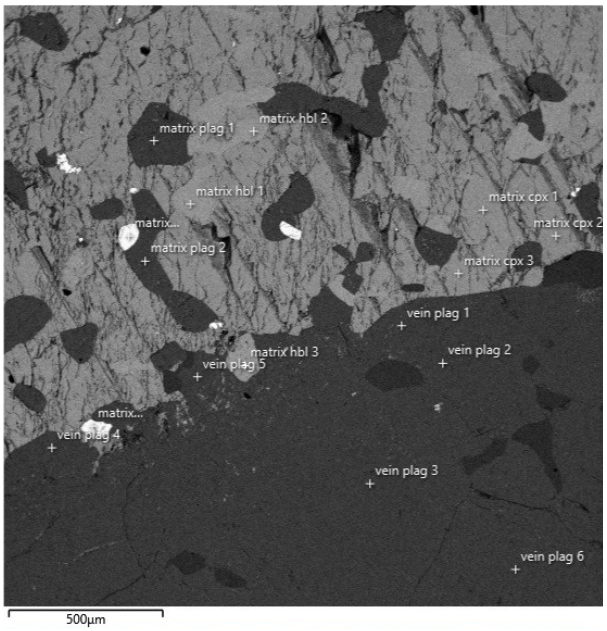

Fig. 16. SEM-image of contact between the qz-plag domain (darker area) and the fine-grained matrix (lighter area) in section T1 (1/2). Abbreviations: plag: plagioclase, hbl: hornblende, cpx: clinopyroxene.

A polished section of the melt accumulation vein T1 (1/2) is dominated by quartz and plagioclase (Fig. 15). The plagioclase in this domain is larger and more abundant in comparison with the quartz crystals (Fig. 17). In the plagioclase crystals there is observed a white texture which were identified in EDS-analyzes to be composed of K-feldspar and the barium (Ba) rich K-feldspar hyalophane (Fig. 18). Accessory phases were found throughout the vein and included K-feldspar, calcite, iron oxides, inclusions high in calcium and aluminum and rare pyroxenes.

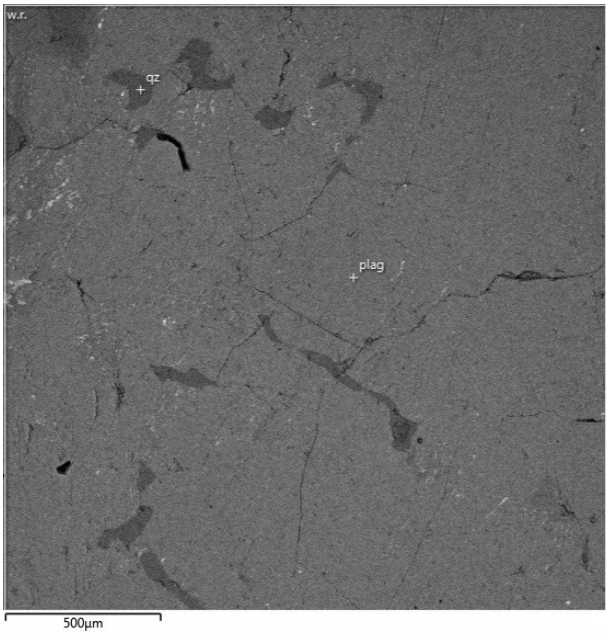

Fig. 17. SEM-image of the melt vein in section T1 (1/2) which shows the larger plagioclase compared to quartz crystals. Abbrevations: plag: plagioclase, qz: quartz.

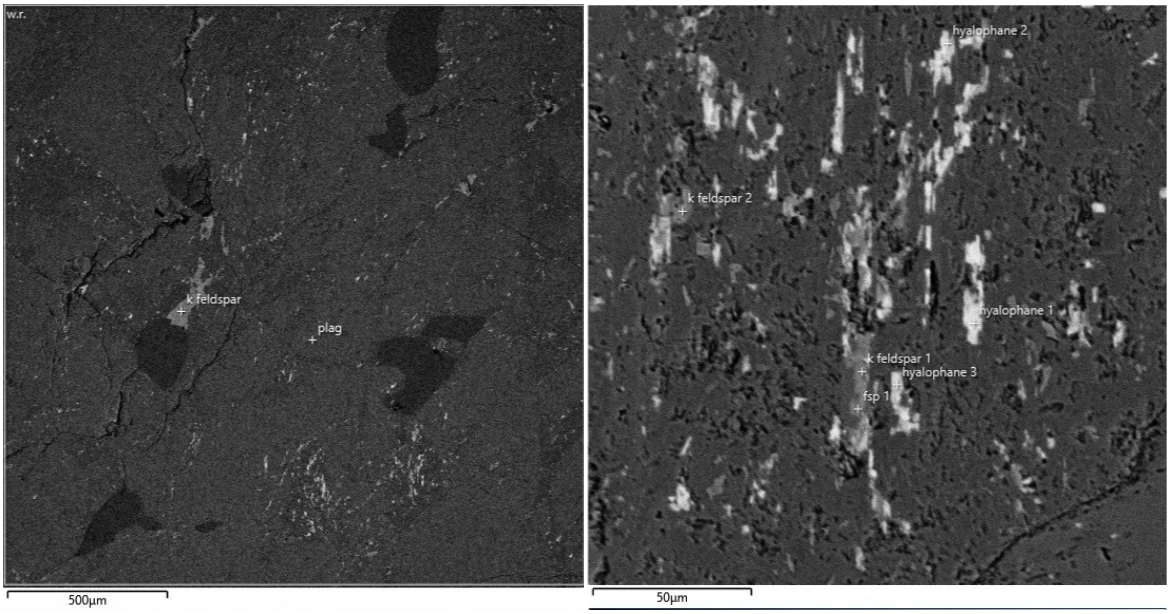

Fig. 18. SEM-images of the melt accumulation vein (section T1 (1/2)) that shows a white texture in the plagioclase crystals (left). Image to the right shows a zoom in the area that through EDS-analyses were identified to be composed of K-feldspar. Abbreviations: fsp: feldspar, plag: plagioclase.

4.3 Mineral chemistry

4.3.1 Plagioclase

The feldspar composition was determined based on amounts of K, Na and Ca, using calculated mean values of data from EDS-analyses in qz-plag areas and matrix domains. The calculation was based on 67 point analyses of plagioclase crystals in the qz-plag areas of section 2A (1/3), 3 (2/3) and 4 (3/5), 39 point analyses of plagioclase crystals in the qz-plag area of section T1 (1/2), 48 point analyses of plagioclase crystals in the hornblende (hbl) matrix of section 2A (1/3), 3 (2/3) and 4 (3/5), and 8 point analyses of plagioclase crystals in the pyroxene (px) bearing matrix of section 3 (2/3) (Appendix IV, V & VI). The results show that plagioclase in the qz-plag domains can be classified as oligoclase (An_{10}-An_{30}), with the melt vein (section T1 (1/2)) showing a lower percentage of anorthite (Fig. 19). The plagioclase in the matrix shows a higher anorthite percentage with an andesine composition (An_{30}-An_{50}) (Fig. 19).

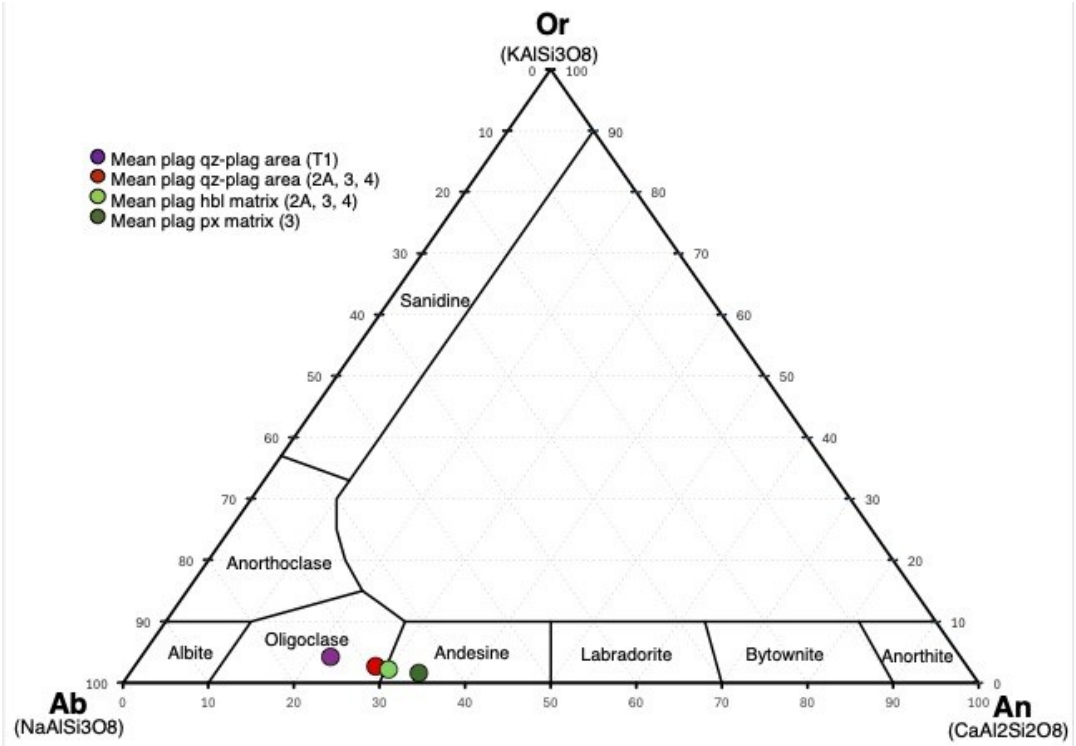

Fig. 19. Feldspar compositional ternary diagram of plagioclase in the qz-plag areas and matrix domains (hbl matrix and px matrix). Calculated mean values of data from EDS-analyses.

4.3.2 Amphibole

Mean values of amphibole composition in the matrix were calculated from 16 point analyses in section 2A (1/3), 9 in section 3 (2/3), 23 in section 4 (3/5) and 6 point analyses in section T1 (1/2) (Appendix VII). Classification of the amphibole were based on element chemistry and was done with calculations of the amphibole data in probe-Amph (Tindle and Webb, 1994). The amphibole in the different sections show a similar composition that is classified to belong in the calcic amphibole group (Table 1). Amphibole composition based on EDS-analyses of 45 amphibole crystals in the hbl matrix of sections 2A (1/3), 3 (2/3) and 4 (3/5), 3 in the px matrix of section 3 (2/3) and 6 analyses in the matrix of section T1 (1/2), were calculated in probe-Amph (Tindle and Webb, 1994) (Appendix VIII). The calculation shows that the dominating amphibole in the matrix of the garnet amphibolite is classified as magnesio-hastingsite ($NaCa_2(Mg_4Fe^{3+})(Si_6Al_2)O_{22}(OH)_2$) (Fig. 20). Two of three analyses in the px-bearing matrix in section 3 (2/3) showed a lower $(Na + K)^A$, with amphibole classified as tschermakite ($Ca_2(Mg_3Al_2)(Al_2Si_6O_{22})(OH)_2$) (Fig. 21). The amphibole in the matrix surrounding the melt accumulation vein were lower in A-site (Na+K) and showed a lower $Mg/(Mg+Fe^{2+})$ ratio, with the dominating amphibole classified as ferro-tschermakite ($Ca_2(Fe^{2+}{}_3Al_2)(Al_2Si_6O_{22})(OH)_2$) (Fig. 21).

Table. 1. Mean values of amphibole composition in the different sections and calculated structural formulae and amphibole calculation scheme in probe-Amph (Tindle and Webb, 1994). The calculations are based on point analyses of amphibole in SEM-EDS that were normalized to a 100 %.

	Mean section 2A (1/3)	**Mean section 3 (2/3)**	**Mean section 4 (3/5)**	**Mean section T1 (1/2)**
Wt. % oxides				
SiO_2	42.51	43.07	42.79	42.18
TiO_2	2.45	2.28	2.31	1.86
Al_2O_3	12.71	12.26	12.57	12.23
FeO	17.25	17.63	17.65	20.94
MnO	0.06	0.07	0.04	0.18
MgO	10.22	10.11	10.04	8.17
CaO	11.28	11.11	11.17	11.32
Na_2O	1.98	1.96	2.00	1.84
K_2O	1.26	1.19	1.19	1.03
P_2O_5	0.01	0.00	0.02	0.04
Total	**99.73**	**99.68**	**99.78**	**99.77**
Atoms per formula unit				
Si	6.205	6.281	6.241	6.242
Al_{iv}	1.795	1.719	1.759	1.758
Al_{vi}	0.392	0.389	0.403	0.375
Ti	0.268	0.250	0.253	0.207
Amphibole calculation scheme				
(Ca + Na) (B)	2.000	2.000	2.000	2.000
Na (B)	0.236	0.265	0.255	0.205
(Na+K) (A)	0.559	0.510	0.532	0.516
$Mg/(Mg+Fe^{2+})$	0.587	0.583	0.580	0.482
$Fe^{3+}/(Fe^{3+}+Al_{vi})$	0.579	0.597	0.586	0.637
Sum of S2	13.000	13.000	13.000	13.000

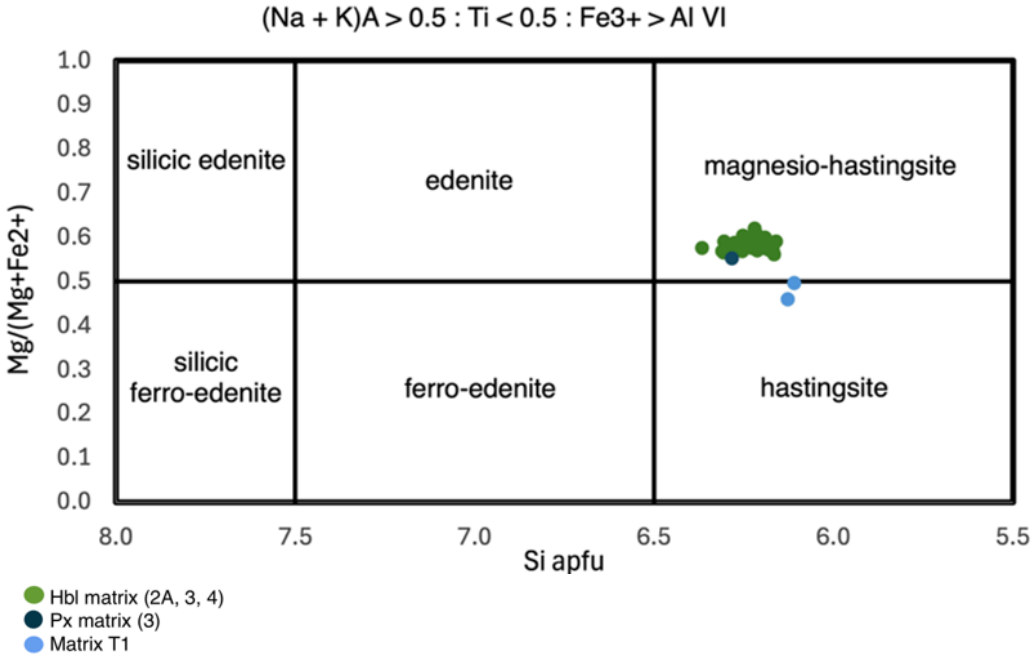

Fig. 20. Amphibole classification diagram of calcic amphiboles with $(Na + K)^A > 0.5$, $Ti < 0.5$ and $Fe^{3+} > Al_{VI}$. Calculations were done in probe-Amph (Tindle and Webb, 1994) with data from EDS-analyses of 44 amphiboles in the hbl matrix of sections 2A (1/3), 3 (2/3) and 4 (3/5), 1 in the px matrix of section 3 (2/3) and 2 analyses in the matrix of section T1 (1/2).

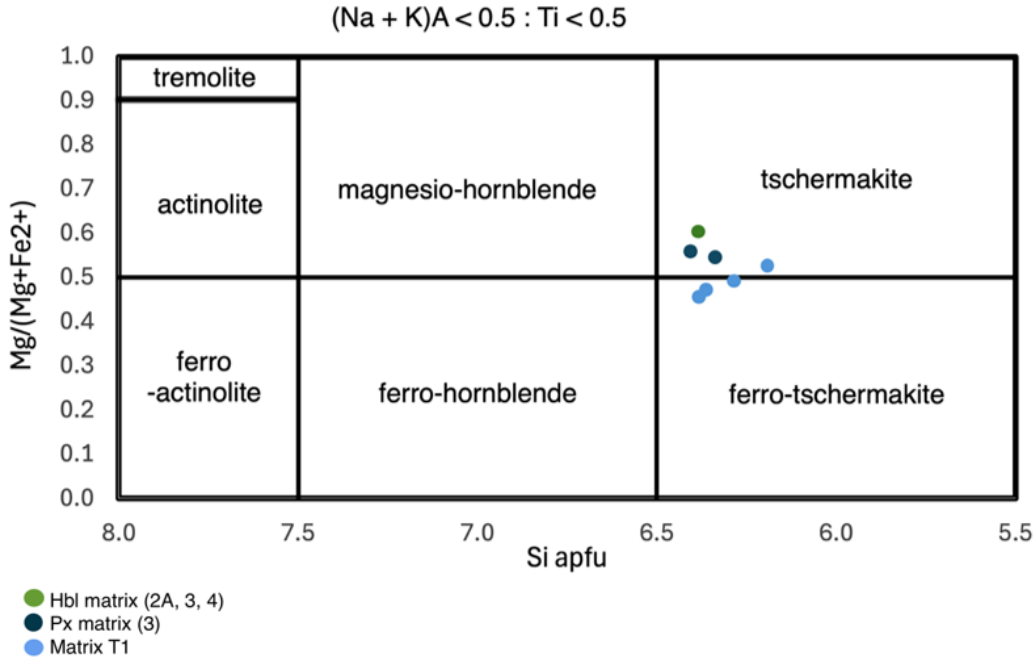

Fig. 21. Amphibole classification diagram of calcic amphiboles with $(Na + K)^A < 0.5$ and $Ti < 0.5$. Calculations were done in probe-Amph (Tindle and Webb, 1994) with data from EDS-analyses of 1 amphibole in the hbl matrix of sections 2A (1/3), 3 (2/3) and 4 (3/5), 2 in the px matrix of section 3 (2/3) and 4 analyses in the matrix of section T1 (1/2).

4.3.3 Garnet

Elemental mapping of garnet porphyroblasts in section 2A (1/3) showed no distinct compositional zonation (Fig. 22).

Mean values of garnet composition were calculated from 3 point analyses in section 2A (1/3), 4 in section 3 (2/3), 4 in section 4 (3/5) and 3 point analyses in section T1 (1/2) (Appendix IX). Calculated proportions of the garnet species pyrope (prp) ($Mg_3Al_2Si_3O_{12}$), spessartine (sps) ($Mn_3Al_2Si_3O_{12}$), almandine (alm) ($Fe_3Al_2Si_3O_{12}$), and grossular (grs) ($Ca_3Al_2Si_3O_{12}$), gave a composition of $Prp_{6.3\text{-}8.3}$ $Sps_{1.3\text{-}4.8}$ $Alm_{61.5\text{-}63.9}$ $Grs_{25.5\text{-}28.8}$. The garnet porphyroblasts showed a similar composition with the dominating garnet species as almandine followed by grossular (Fig. 23).

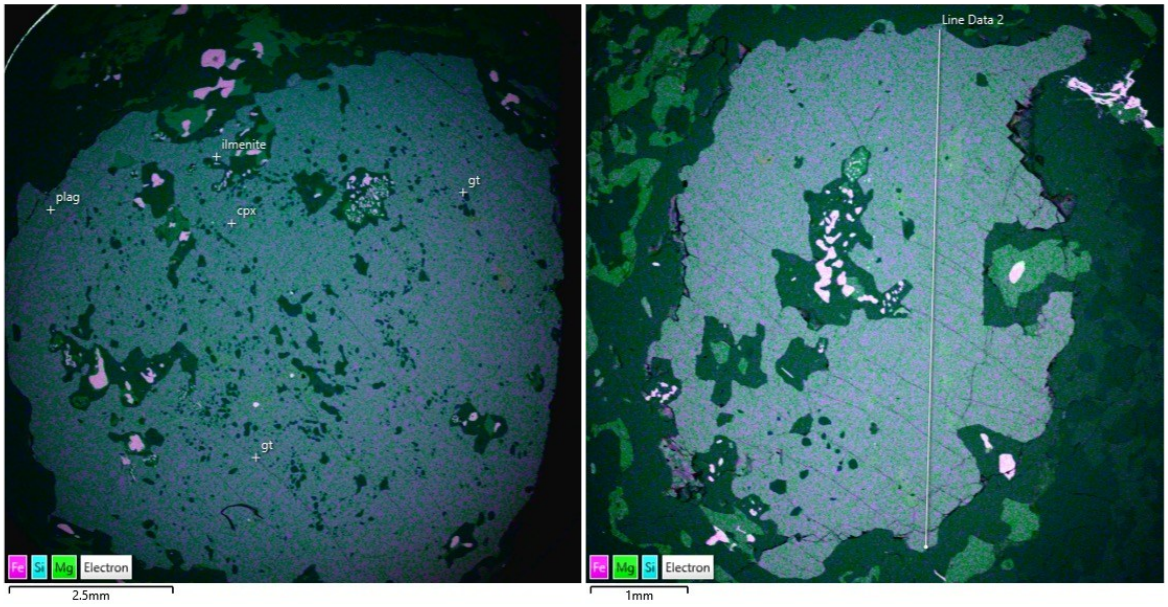

Fig. 22. Elemental mapping in EDS-analysis of garnet porphyroblasts in section 2A (1/3).

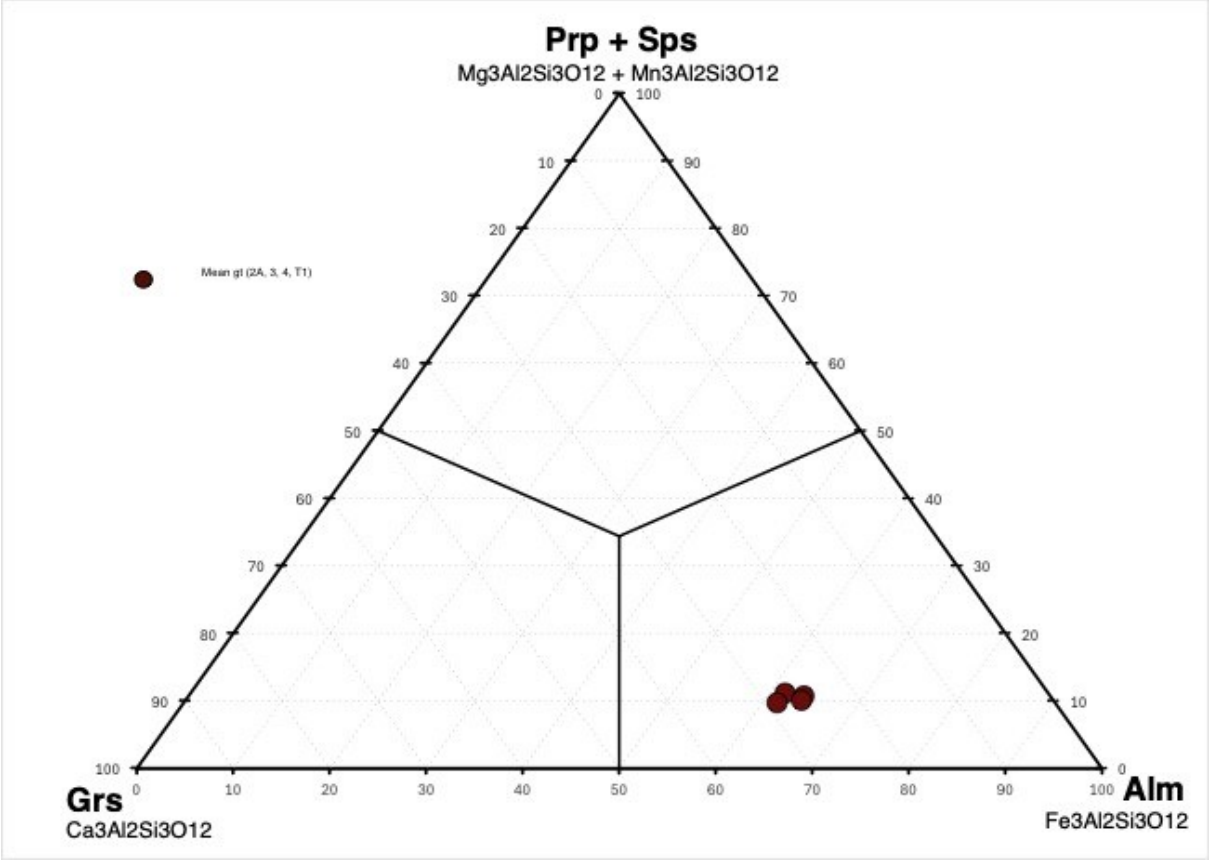

Fig. 23. Garnet compositional ternary diagram of endmembers pyrope + spessartine, grossular and almandine. Dots represent calculated mean values for garnet in the different sections of data from EDS-analyses.

4.4 Major element geochemistry

Variation diagrams were plotted using GCD-kit (Janousek et al., 2006) with data collected from EDS point- and area analyses of the qz-plag areas and matrix (see Appendix II & III for placement). Diagrams with data from the qz-plag areas, matrix domains and of the dominating minerals in the different sections were plotted against major elements (Fig. 24, 25, 26, Appendix X & XI). Mean values of the different domains were calculated for each section based on analyses of 2000x2000 µm square areas. The calculation of mean qz-plag area composition was based on 8 areas in section 2A (1/3), 4 in section 3 (2/3), 7 in section 4 (3/5) and 19 areas in section T1 (1/2) (Appendix XII). The calculation of the mean hbl bearing matrix was based on 8 areas in section 2A (1/3), 3

areas in section 3 (2/3) and 8 areas in section 4 (3/5). The calculation of px bearing matrix was based on 4 areas in section 3 (2/3) (Appendix XIII). The diagrams for the sections from the garnet amphibolite (2A (1/3), 3 (2/3) and 4 (3/5)), show similar major elements concentrations and a trend in the data of the qz-plag areas that extends between plagioclase and quartz (Fig. 24 & 25). This trend is absent in the diagram of the melt accumulation vein (section T1 (1/2)), where the data of the qz-plag areas show a higher Na_2O and Al_2O_3 that plots near the plagioclase composition (Fig. 24 & 25). By the diagrams it is also visible that the px bearing matrix were analyzed in section 3 (2/3) alone and that this section has a higher percentage of observed clinopyroxene. It is also possible to see that K-feldspar only were observed in the melt accumulation vein (section T1 (1/2)).

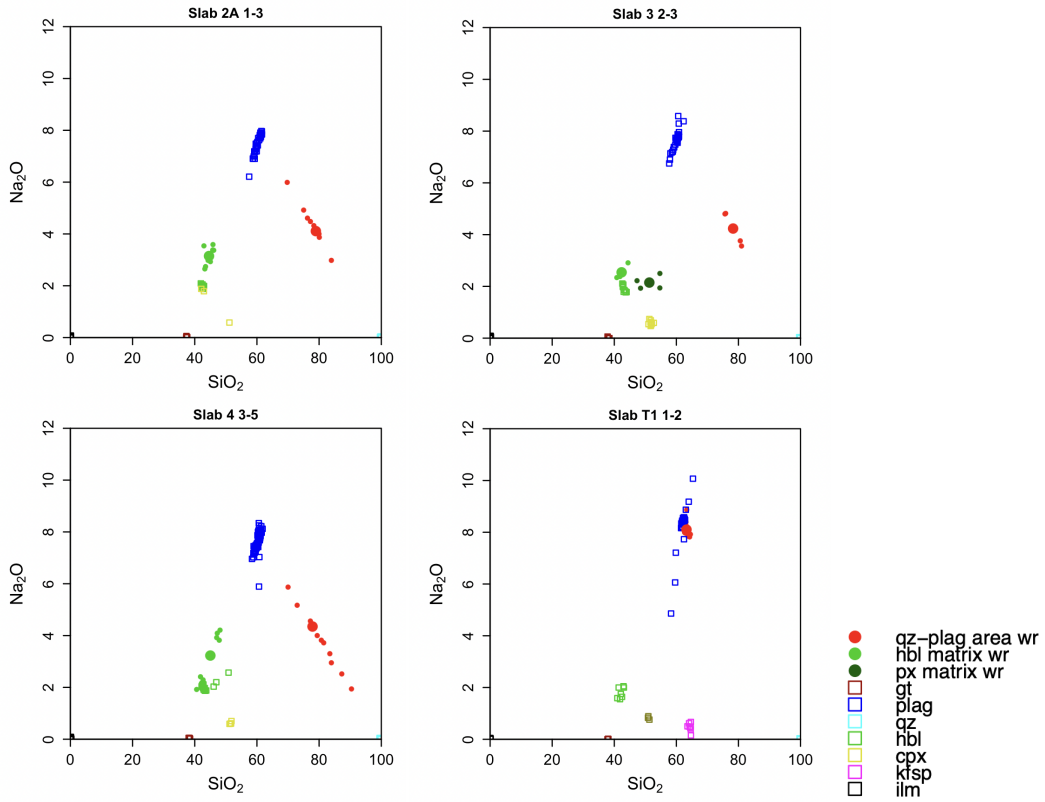

Fig. 24. Harker diagram with SiO_2 plotted against Na_2O of the qz-plag area, matrix domains and the dominating minerals for the different sections. The mean values of the qz-plag areas and matrix domains are shown as larger dots. Plotted in GCDkit (Janousek et al., 2006). Abbreviations: wr: whole rock, hbl: hornblende, px: pyroxene, gt: garnet, plag: plagioclase, qz: quartz, cpx: clinopyroxene, kfsp: K-feldspar, ilm: ilmenite.

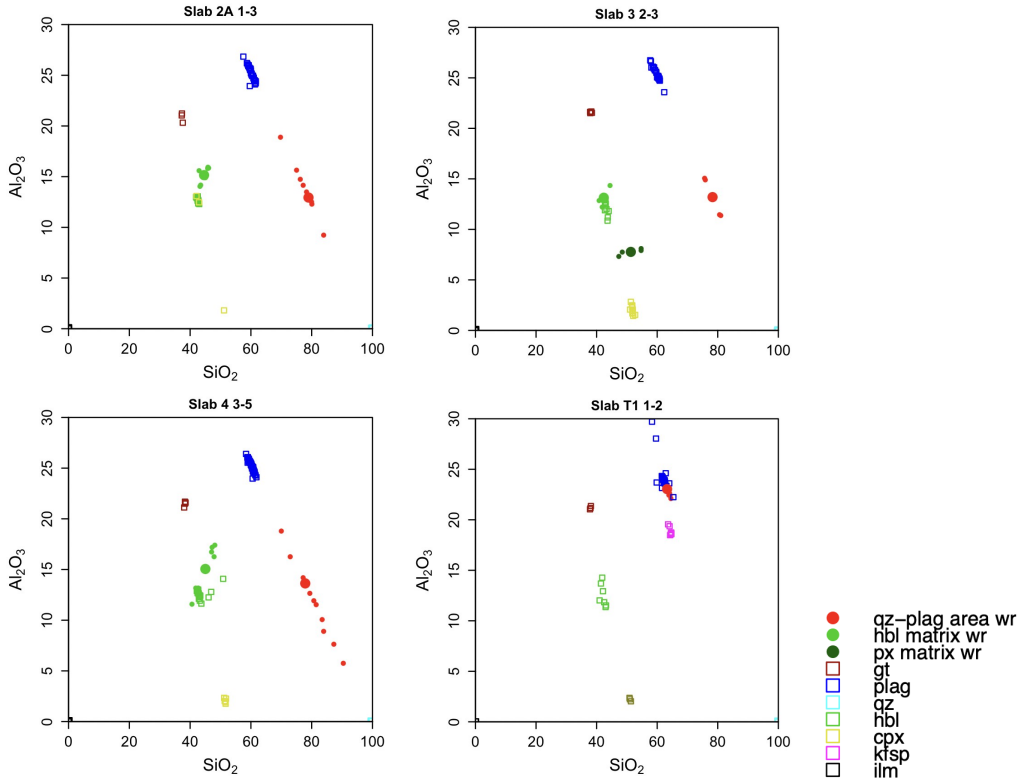

Fig. 25. Harker diagram with SiO_2 plotted against Al_2O_3 of the qz-plag area, matrix domains and the dominating minerals for the different sections. The mean values of the qz-plag areas and matrix domains are shown as larger dots. Plotted in GCDkit (Janousek et al., 2006). Abbreviations: wr: whole rock, hbl: hornblende, px: pyroxene, gt: garnet, plag: plagioclase, qz: quartz, cpx: clinopyroxene, kfsp: K-feldspar, ilm: ilmenite.

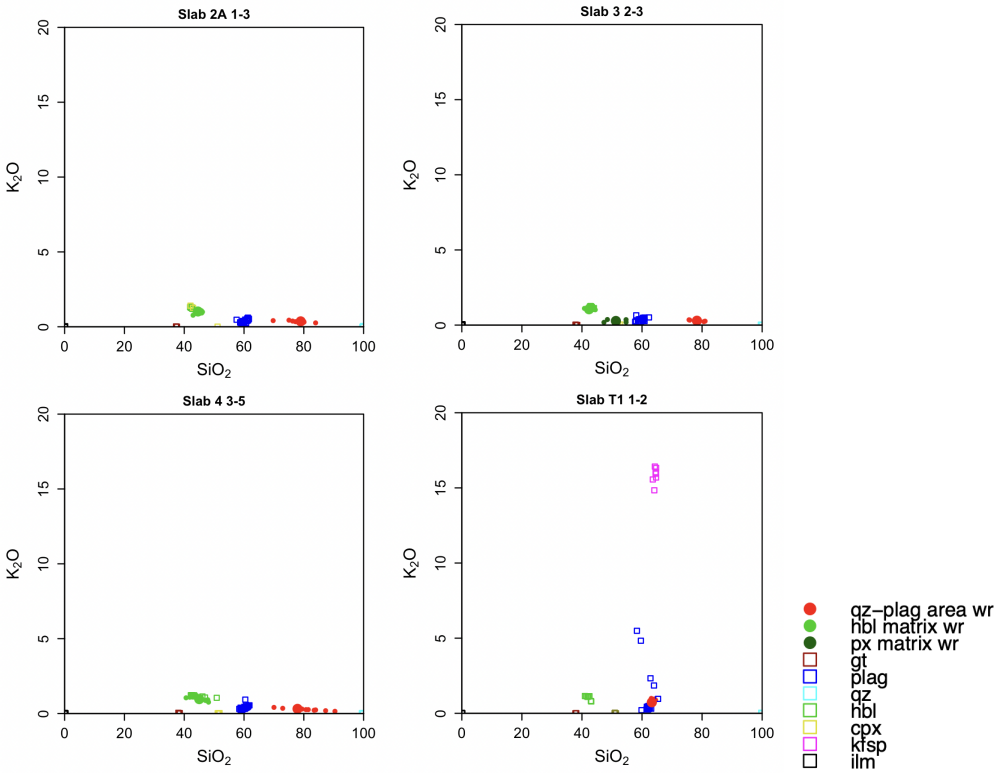

Fig. 26. Harker diagram with SiO_2 plotted against K_2O of the qz-plag area, matrix domains and the dominating minerals for the different sections. The mean values of the qz-plag areas and matrix domains are shown as larger dots. Plotted in GCDkit (Janousek et al., 2006). Abbreviations: wr: whole rock, hbl: hornblende, px: pyroxene, gt: garnet, plag: plagioclase, qz: quartz, cpx: clinopyroxene, kfsp: K-feldspar, ilm: ilmenite.

5 Discussion

5.1 Quartz-plagioclase areas

5.1.1 Indications of partial melting

Tonalitic areas in a mafic rock can form through partial melting, but the occurrence of quartz and plagioclase rich domains surrounding garnet can also be explained through element depletion as the garnet crystals grow. In the sections from the garnet amphibolite the qz-plag areas are often observed near garnet, but they are also present in the matrix without contact to the garnet porphyroblasts. Additionally, the qz-plag areas near the garnet are commonly located along opposite sides of the garnet, in areas that appears to follow stress shadows parallel with the general fabric (Fig. 6 & 7). If the qz-plag areas were the result of element depletion they would rather be growing around the garnet (Winter, 2014). The distribution of these domains might therefore indicate that the areas are not generated through depletion from garnet growth, but rather being the result of partial melting. This interpretation is further strengthened by the inclusions of hornblende found in the qz-plag areas, which would be unlikely to be present in depletion rims as hornblende are composed of elements (Fe and Mg) that are consumed to form garnet (Winter, 2014). These observations corroborate the assumption that the qz-plag rich domains in the garnet amphibolite is a result of partial melting. However, one thing that questions this is the very low concentration of K in these areas (Fig. 26). This relates to that K is an incompatible element and would therefore favorably be enriched in the melt phase (Winter, 2014). So, although many arguments suggest that partial melting has occurred this must still be considered and would require further studies to fully determine for certain.

5.1.2 Differences between the samples

The geochemical analyses of the qz-plag areas shows a variation between the sections from the garnet amphibolite (2A (1/3), 3 (2/3) and 4 (3/5)) and the melt accumulation vein (T1 (1/2)). In the major element diagrams with SiO_2 plotted against Na_2O and Al_2O_3 (Fig. 24 & 25), the analyses of the qz-plag areas in sections from the garnet amphibolite shows a linear trend spanning between pure plagioclase and quartz which indicates that the composition is dominated by the mixture between these minerals. The variation shown in the data are a result of the amount and size of respective crystals in the different analyzed square areas. A mixing trend is absent in the diagrams of section T1 (1/2) from the melt accumulation vein, where the qz-plag area have a Na_2O and Al_2O_3 concentration close to plagioclase (Fig. 24 & 25). This difference is explained by the larger and more abundant plagioclase compared to quartz crystals of the melt vein (Fig. 17), which results in the higher percentage of Na_2O, Al_2O_3 and a lower amount of SiO_2 (Fig. 24 & 25).

The courser texture in section T1 (1/2) (compare Fig. 9 & Fig. 17) could have several explanations such as variations in time, crystallization pace or in the presence of fluids (Winter, 2014). A longer crystallization time that would allow the crystals to grow larger could arise if the melt accumulation vein was generated at a higher temperature (Winter, 2014), something that also could lead to more extensive melting which would explain the larger amount of melt. However the different samples were most likely exposed for the same temperature as their different textures are observed in close distance at the amphibolite outcrop, which most probably were affected by similar conditions. The melt vein would more likely be a sign of melt separation from the matrix, caused by progressive melting generating the critical amount of melt needed for this to occur. A difference in the degree of melting could explain the variations in the melt volume between the samples, by melt segregation leading to the accumulation of a larger amount of melt. Accumulation of a larger amount of melt could then possibly result in a lower cooling rate that would have an effect on crystallization and generate a coarser texture (Winter, 2014). Melting experiments of amphibolite has also shown that as temperature exceeds 900 °C, the liquid composition will decrease in SiO_2 and increase in Al_2O_3 and Na_2O (Wolf & Wyllie, 1994). As the melt vein has a lower percentage of SiO_2 and higher Al_2O_3 and Na_2O compared to the qz-plag areas in the garnet amphibolite (Fig. 24 & 25), this might further indicate progressive melting.

The inclusions in the qz-plag domains also varied between the garnet amphibolite and the melt accumulation vein sample. The qz-plag areas of the garnet amphibolite are dominated by Ti-bearing inclusions (ilmenite, titanite, and Ti-oxides) which were lacking in the melt vein. If Ti was incorporated in the liquid early, in concentrations that would cause the crystallization of Ti-bearing minerals, this could possibly indicate that melt segregation has occurred with earlier formed liquid of the melt accumulation vein. However, further studies and analyses of trace elements would be required to fully determine if melt has left the system.

K-feldspar was frequently observed as a white texture in the plagioclase crystals of the melt domain in section T1 (1/2) and a closer zoom on the K-feldspar shows a vague orientation of the crystals that could possibly be described as lamellae caused by exsolution (Fig. 18). The K enriched area of a plagioclase crystal observed in the qz-plag area of section 2A (1/3) shows a similar texture but more homogeneous, with no clear orientation (Fig. 12). This could indicate a faster cooling without the time to develop an exsolution lamellae texture (Winter, 2014). A difference in cooling rate has an effect on crystallization and the observations indicating a possible slower cooling of the melt vein would generate a coarser texture (Winter, 2014).

Despite the suggestion that various degrees of melting could be the cause of the difference in grain size between the samples, the plagioclase crystals in the melt accumulation vein are more Na rich than the garnet amphibolite sample which stands in contrast to more extensive melting that would lead to a higher Ca content (Winter, 2014). The higher pressure that the area was affected by during the orogeny could explain a lower Ca, as experiments has shown an enrichment in Na for high-pressure melts (Moyen & Stevens, 2006; Moyen, 2011). Although this can't explain the difference between the samples, where a progressive melting generating the melt vein would naturally lead

to a higher Ca compared to the qz-plag areas, which is not the case. It should also be noted that the size variation between the plagioclase and quartz crystals in the melt vein possibly could be the result of the orientation in which the sample was cut – cutting along the plagioclase crystals and across the quartz crystals making them appear smaller. The two-dimensional sampling area would then not be representative of the vein volume mode. These arguments therefore limit the interpretation if the variations between the samples could have been caused by a difference in the degree of melting.

5.1.3 Field observations

Domains of quartz and plagioclase occurred in the garnet amphibolite outcrop as smaller patches, bands and larger accumulations (Fig. 4, 5 & 6). These observations of a difference in volume of the qz-plag areas, might strengthen that the melt vein and qz-plag areas in the garnet amphibolite sample are related and generated through the same process. This would then exclude that the melt vein is composed of melting material with a different origin that had migrated in and intruded the outcrop. The differences in volume of the qz-plag areas could relate to a variation in the degree of melting as discussed above to be a possible explanation to the coarser texture of the melt vein. Although why the degree of melting would vary over the outcrop is debatable. It could possibly relate to deformation, as observations showed that areas of the outcrop seemed to have experienced a higher strain, where garnet was oriented in lineation (Fig. 4 & 5). The larger melt accumulations and veins appears to be concentrated to these possibly more deformed areas, while more isolated pockets of melt instead seem to occur in less deformed areas of the garnet amphibolite (Fig. 4, 5 & 6). A higher grade of deformation could potentially lower the amount of melt needed for melt segregation by strain causing melt pockets to connect. Although it should be noted that a more extensive study of the outcrop and the possibility of a variation in deformation is needed.

5.2 Amphibolite matrix

5.2.1 Indications of partial melting

A difference between the samples is visible in the matrix, where the finer grained matrix is more abundant in the melt accumulation vein sample compared to the areas with larger hornblende crystals which dominates the matrix in the garnet amphibolite (Fig. 7, 14 & 15). The finer grained pyroxene bearing areas were only analyzed in section 3 (2/3) where it made up a large concentration of the matrix, which in the other sections were dominated by larger hornblende and plagioclase crystals. But areas that shows a similar textural character as these finer-grained areas, with low macroscopic hornblende crystals, can be observed in smaller amounts in the other sections, especially in section 2A (1/3) where it is clearly distributed near the qz-plag areas and garnet (Fig. 7). The matrix in the melt vein sample is dominated by this finer grained texture without macroscopic hornblende (Fig. 14 & 15), and EDS-analyses in an area of the matrix in section T1 (1/2) shows the presence of clinopyroxene (Fig. 16). This would imply a similar composition as the pyroxene bearing matrix in section 3 (2/3), but further examination of the matrix in section T1 (1/2) are required to give a more careful comparison, as only a few analyses were carried out due to the section being largely covered by the melt vein. These observations could be indicative of partial melting in the rock, as dehydration-melting of amphibolite causes hornblende to break down to clinopyroxene with the release of water that initiate the formation of granitoid liquids (Wolf & Wyllie, 1991; Zhang et al., 2013). This could explain why the areas of the matrix close to the qz-plag domains are depleted of large hornblende crystals and clinopyroxene is present. It would also explain why the matrix surrounding the melt accumulation shows this character to a larger extent, as the larger amount of melt would require a more extensive dehydration of hornblende. The variations in the matrix can give indications of the temperature and pressure during melting, as melting experiments at 10 kbar have shown that breakdown of hornblende and the formation of clinopyroxene and liquid starts at 850 °C (Wolf & Wyllie, 1991). As temperature increases the amount of clinopyroxene and liquid increases and hornblende decreases (Wolf & Wyllie, 1991). The breakdown of hornblende through dehydration melting can also cause garnet to form along with the clinopyroxene (Wolf & Wyllie, 1994; Zhang et al., 2013), and this might be indicated by the inclusions in the garnet. The inclusions were often observed as a symplectite texture of plagioclase, clinopyroxene and vermicular ilmenite crystals intergrown together. The plagioclase and clinopyroxene are probably remnants of the matrix that were enclosed as the garnet grew and the absence of hornblende could indicate that the garnet formed with the breakdown of hornblende. Inclusions of quartz were also found in the garnet which might imply that they grew as the rock underwent partial melting, as quartz was absent in the dominating amphibolite matrix.

5.2.2 Implications on conditions

Experimental work shows that the appearance of garnet and clinopyroxene with the breakdown of hornblende, occur at temperatures over 850 °C at a pressure of 10 kbar (Wolf & Wyllie, 1994). Further indications of temperature and pressure (P-T) conditions can be given by observations in the amphibolite matrix. The presence of garnet and absence of epidote indicates a high pressure above 10 kbar and temperature over 800 °C (Lopez & Castro, 2001). The lack of zonation in garnet could also be explained by a high temperature (>650 °C) with a more effective volume diffusion that would cause any early zoning to be eliminated (Yardley, 1989). However, it should be noted that only two garnets were analyzed in one of the sections through elemental mapping and further analyzes are required for a more careful interpretation of zonation. Ti-buffering minerals (ilmenite, rutile or titanite), were present in the matrix and the amphibole composition with a Ti-content over 0.2 atom per formula unit (Table 1) indicate crystallization temperatures that might exceed 800 °C (Bartoli et al., 2024). Al-content in amphibole is largely temperature dependent and can only give an indicative estimate of pressure, but the

Al^{Tot} in the amphibole might suggest a hornblende crystallization pressure of around 7 kbar at a temperature of 700 °C (Blundy & Holland, 1990). These estimates can provide a tentative indication that the rock was affected by P-T conditions in the supersolidus regime (Lopez & Castro, 2001), but a more careful P-T analysis is beyond the scope of this study.

5.3 Comparison to TTG

5.3.1 Mineralogy

TTG rocks are believed to have been derived through partial melting of meta-basalts but there still is an uncertainty in the understanding of their origin. The mineralogy of the melt domains in the garnet amphibolite, composed of quartz and plagioclase, is comparable to TTG composition. Biotite is a common mineral in TTG rocks and its absence in the qz-plag areas could relate to the low concentration of K_2O, MgO and FeO in the rock. By plotting the mean composition of the qz-plag areas against average TTGs in a normative feldspar diagram, the melt domains in the garnet amphibolite (section 2A (1/3), 3 (2/3) and 4 (3/5)) are tonalitic while the melt accumulation vein represented by section T1 (1/2) is more trondhjemitic (Fig. 27). The diagram also highlights the very low K_2O-content of the qz-plag areas compared to TTGs, shown by the lack of orthoclase ($KAlSi_3O_8$). The plagioclase composition of the qz-plag areas that were classified as oligoclase (Fig. 19), is however comparable to TTG, as it is the dominating plagioclase found in these rocks.

5.3.2 Major element composition

The major element trend of the qz-plag areas with a high SiO_2 and Na_2O, and low K_2O is characteristic for TTG, but some divergence in concentrations can be observed (Fig. 28). The qz-plag areas in the garnet amphibolite shows a higher SiO_2 of ~ 75-80 wt. % compared to average TTG where the amount lays around 65-70 wt. %. Section T1 (1/2) has a lower SiO_2 concentration of ~ 60-65 wt. %, which can be assumed to be caused by the larger and more abundant plagioclase crystals of the melt vein. If it is assumed that the melt accumulation vein was generated through more extensive melting than the melt domains of the garnet amphibolite, the variation in SiO_2 could be argued to be related to the degree of melting. The larger more abundant plagioclase crystals in section T1 (1/2) are also the cause of its high Na_2O and Al_2O_3 that deviates from average TTG composition (Fig. 28). In contrast are the Na_2O and Al_2O_3 concentrations of the qz-plag areas in the garnet amphibolite comparable to concentrations in TTG. The K_2O of the qz-plag areas is very low (<1.0 wt. %) and deviates from average TTG (Fig. 28). K is an incompatible element that would likely partition into the melt phase and the lack of this element in the qz-plag areas could imply a residual mineral that retains K. As K_2O is almost as low (≈1 wt. %) in the matrix (Fig. 26), it might also be explained by the lack of this element in the source rock. This could indicate that the variation in K from TTG composition is related to the source composition

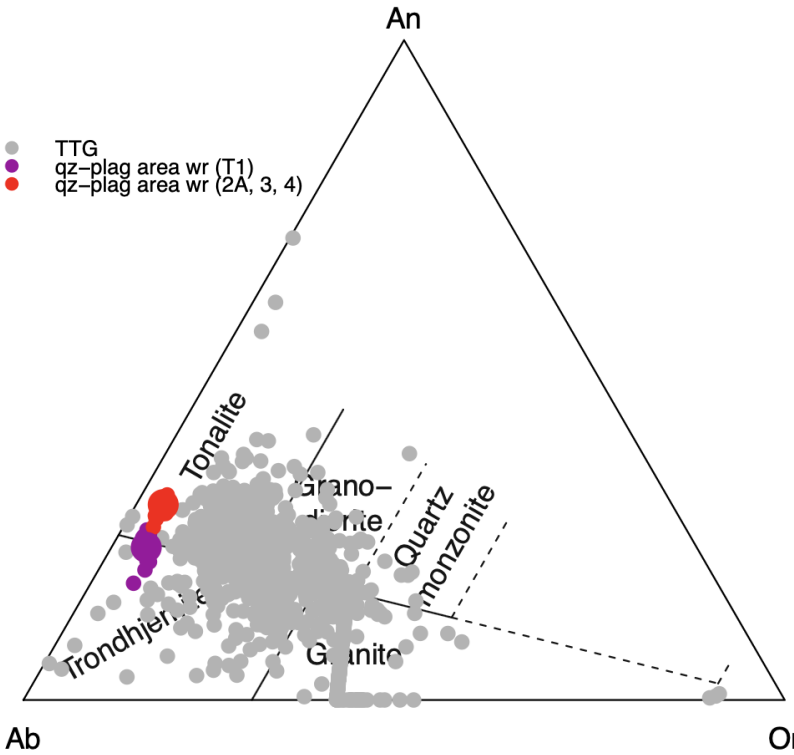

Fig. 27. Feldspar composition triangle (O'Connor 1965) of TTG and data from EDS-analyses of the qz-plag areas plotted in GCDkit (Janousek et al., 2006). The mean values of the qz-plag domains are shown as larger dots. TTG data is composed of 172 trondhjemite samples, 304 tonalite samples and 277 granodiorite samples (Data were downloaded from the GEOROC database (https://georoc.eu/) on 1-2 April 2026, using the following parameters: geological setting = Archean Cratons). The data were normalized using CIPW calculation in GCDkit. Abbreviations: TTG: trondhjemite tonalite granodiorite, qz: quartz; plag: plagioclase; wr: whole rock; Ab: albite, An: anorthite, Or: orthoclase.

rather than being caused by different melting processes. The lower K_2O together with the absence of biotite in the garnet amphibolite could then possibly imply that TTG-melts are derived from a source rock with higher K-content.

5.3.3 Formation processes

The qz-plag areas in the garnet amphibolite exhibit the main characteristic of TTGs with a mineralogy of quartz and oligoclase, and a geochemical signature high in SiO_2 (> 70 wt. %) and Na_2O (2.0-6.0 wt. %), and low in K_2O (<1.0 wt. %). Although on the fringe, with the high SiO_2 and low K_2O, the qz-plag areas in the garnet amphibolite sample still plot within the Archean TTG population (Fig. 28), which could suggest that they are derived through similar processes. The garnet amphibolite outcrop is located in the Eastern Segment, which were affected by the Sveconorwegian orogeny through underthrusting and orogenic crustal thickening (Bingen et al., 2021). With regard to the tectonic setting and conditions present in the generation of the garnet amphibolite, this suggest that the formation of TTG-melts can be achieved through intracrustal melting without the need of an extensive subduction zone or possibly subduction setting at all. It is also necessary to consider the higher geothermal gradient in the Archean that could have an effect on where melting occurs and possibly also the extent of melting, depending on tectonic setting (Martin, 1986; Frost & Mueller, 2024). Variations in conditions, with a higher temperature at a lower pressure, could also initiate partial melting of amphibolite at a lower temperature (Lopez & Castro, 2001). These factors could then potentially be an explanation for the differences between the qz-plag areas and TTG, but would require further studies to interpret more carefully.

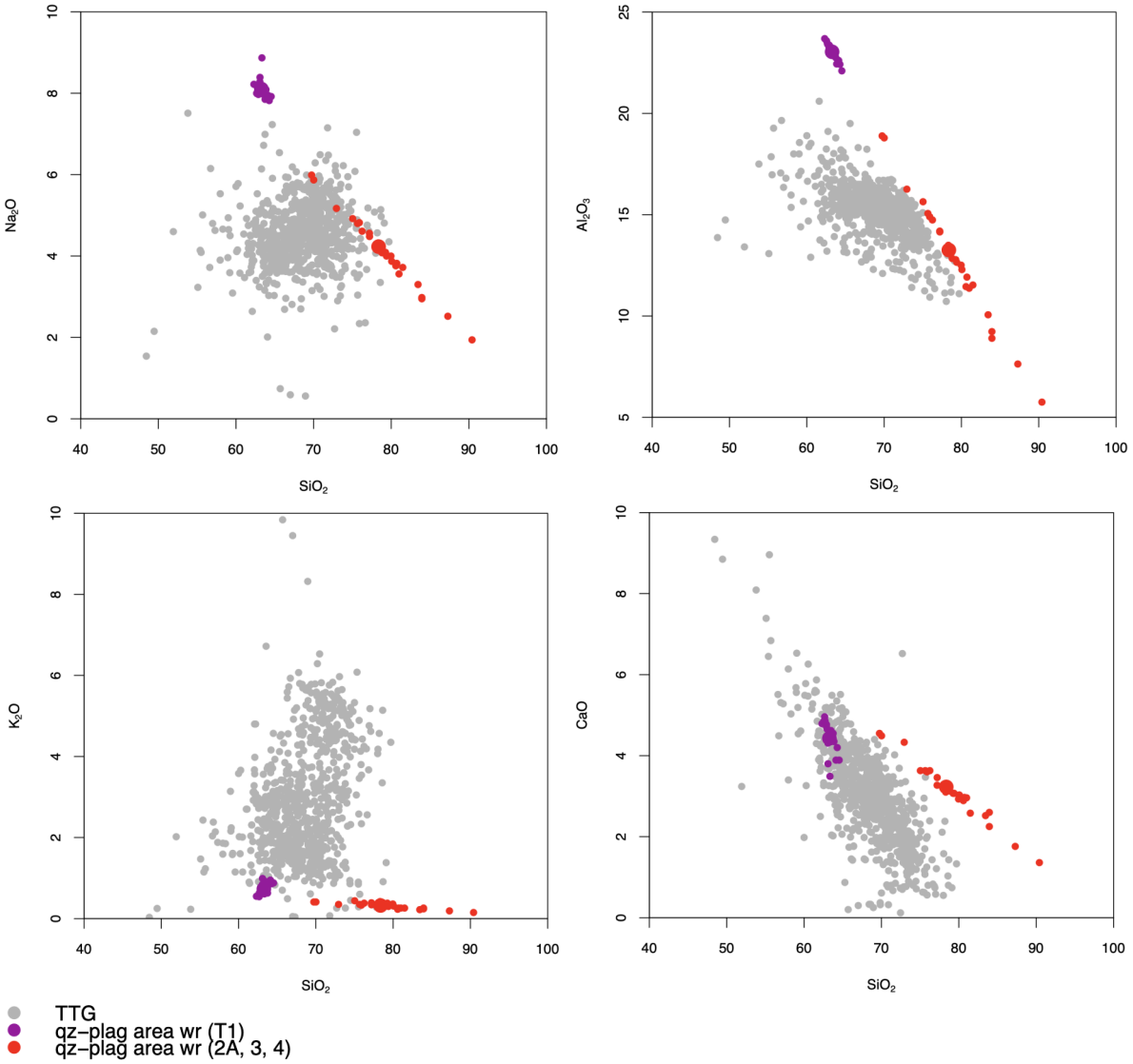

Fig. 28. Harker diagrams of TTG and data from EDS- analyses of the qz-plag areas plotted in GCDkit (Janousek et al., 2006). The mean values of the qz-plag domains are shown as larger dots. TTG data is composed of 172 trondhjemite samples, 304 tonalite samples and 277 granodiorite samples (Data were downloaded from the GEOROC database (https://georoc.eu/) on 1-2 April 2026, using the following parameters: geological setting = Archean Cratons). Abbreviations: TTG: trondhjemite tonalite granodiorite, qz: quartz; plag: plagioclase; wr: whole rock.

6 Suggestions for further studies

- Further geochemical analyses with improved major elements data but also of trace elements (both SEM and drilled microsamples of melt areas) would enable a more detailed understanding of the melting processes. Laser Ablation ICP-MS analyses of trace elements in the qz-plag areas and matrix domains would enable a more extensive comparison to TTG and could give a deeper insight into the conditions during melting.
- A more extensive P-T analysis would enable better estimates on conditions during melting that can help in the constraints of TTG formation.
- Further examination of the melt accumulation vein by analyses of the melt mineralogy in more dimensions and additional studies of the composition in the surrounding matrix. This would enable a more careful interpretation of the difference between the two samples and related conditions, which in turn can be used to better understand the formation of TTG.
- Dating of zircons in the garnet amphibolite would confirm the assumed intrusion and metamorphic age of the rock.

7 Conclusions

- Observations of the quartz and plagioclase areas are compatible with an origin through partial melting of the garnet amphibolite, as the distribution of the domains in the rock and the inclusions of hornblende crystals indicates that they are not formed through element depletion during garnet growth. The variation in the matrix with finer-grained clinopyroxene bearing areas, is also interpreted to be the result of dehydration melting, where hornblende breaks down to clinopyroxene with the release of water that initiate liquids to form.
- The variation showed by the sections of the garnet amphibolite sample (2A (1/3), 3 (2/3) and 4 (3/5)) and the melt accumulation vein sample (T1 (1/2)), is interpreted to represent various degrees of melting that could generate the larger accumulation of melt and coarser texture of the melt vein.
- The presence of garnet, absence of epidote, Ti-content in amphibole and the clinopyroxene bearing areas of the matrix, suggests temperatures above 850 °C and pressures over 10 kbar, indicating conditions in the supersolidus regime.
- The quartz and plagioclase mineral assemblage and high SiO_2 (> 70 wt. %), high Na_2O (2.0-6.0 wt. %), and low K_2O (<1.0 wt. %) of the melt domains confirms that they correspond to K-poor tonalite and that they are comparable to TTG.
- The area with the garnet amphibolite outcrop was affected by orogenic crustal thickening during the Sveconorwegian orogeny, and based on this the results imply that TTG-melts can form through intracrustal partial melting of garnet amphibolite, under conditions that doesn't require an extensive subduction zone.

8 Acknowledgements

I would like to thank my supervisor Anders Scherstén for introducing me to this interesting subject and giving me the opportunity to undertake this study. I wish to sincerely thank you for your guidance and continued enthusiasm throughout this project. I would also like to express my gratitude to Chris Hawkesworth for showing interest in this project. I wish to thank Tomas Næraa and Andreas Petersson for your help with the sample preparation. Lastly, I would like to thank my friends and family for encouraging me during this time.

9 References

Barker, F. (1979). Chapter 1 - Trondhjemite: Definition, Environment and Hypotheses of Origin. Developments in Petrology, 6, 1-12. https://doi.org/10.1016/B978-0-444-41765-7.50006-X

Barker, F., Arth, J. G., & Hudson, T. (1981). Tonalites in crustal evolution. Philosophical Transactions of the Royal Society A, 301, 293-303. https://doi.org/10.1098/rsta.1981.0112

Bartoli, O., Carvalho, B. B., & Farina, F. (2024). Effectiveness of Ti-in-amphibole thermometry and performance of different thermometers across lower continental crust up to UHT metamorphism. Contributions to Mineralogy and Petrology, 179. https://doi.org/10.1007/s00410-024-02149-6

Bingen, B., Nordgulen, Ø., & Viola, G. (2008). A four-phase model for the Sveconorwegian orogeny, SW Scandinavia. Norwegian journal of geology, 88, 43-72.

Bingen, B., Viola, G., Möller, C., Vander Auwera, J., Laurent, A., & Yi, K. (2021). The Sveconorwegian orogeny. Gondwana Research, 90, 273-313. https://doi.org/10.1016/j.gr.2020.10.014

Blundy, J. D., & Holland, B. J. T. (1990). Calcic amphibole equilibria and a new amphibole-plagioclase geothermometer. Contributions to Mineralogy and Petrology, 104, 208-224. https://doi.org/10.1007/BF00306444

Davies, F. G. (1992). On the emergence of plate tectonics. Geology, 20, 963-966. https://doi.org/10.1130/0091-7613(1992)020<0963:OTEOPT>2.3.CO;2

Frost, C. D., & Mueller, P. A. (2024). Archean Cratons: Time Capsules of the Early Earth. Elements, 20, 162-167. https://doi.org/10.2138/gselements.20.3.162

Van Hunen, J., & van den Berg, A. P. (2008). Plate tectonics on the early Earth: Limitations imposed by strength and buoyancy of subducted lithosphere. Lithos, 103, 217-235. https://doi.org/10.1016/j.lithos.2007.09.016

Janousek, V., Farrow, C. M., & Erban, V. (2006). Interpretation of Whole-rock Geochemical Data in Igneous Geochemistry: Introducing Geochemical Data Toolkit (GCDkit). Journal of Petrology, 47, 1255-1259. https://doi.org/10.1093/petrology/egl013

Johansson, L., & Kullerud, L. (1993). Late Sveconorwegian metamorphism and deformation in southwestern Sweden. Precambrian Research, 64, 347-360. https://doi.org/10.1016/0301-9268(93)90087-I

Johnson, T. E., Brown, M., Gardiner, N. J., Kirkland, C. L., & Smithies, R. H. (2017). Earth's first stable continents did not form by subduction. Nature, 543, 239-242. https://doi.org/10.1038/nature21383

Korchinski, D., Duereth, J., McNeil, R., Au, M., & Schmid, V. (2019). A Brief Introduction to Scanning Electron Microscopy. The University of British Columbia.

Lopez, S., & Castro, A. (2001). Determination of the fluid-absent solidus and supersolidus phase relationships of MORB-derived amphibolites in the range 4-14 kbar. American Mineralogist, 86, 1396-1403. https://doi.org/10.2138/am-2001-11-1208

Martin, H. (1986). Effect of steeper Archean geothermal gradient on geochemistry of subduction-zone magmas. Geology, 14, 753-756. https://doi.org/10.1130/0091-7613(1986)14<753:EOSAGG>2.0.CO;2

Moyen, J. -F., & Stevens, G. (2006). Experimental Constraints on TTG Petrogenesis: Implications for Archean Geodynamics. Archean Geodynamics and Environments, 164. https://doi.org/10.1029/164GM11

Moyen, J. -F. (2011). The composite Archean grey gneisses: Petrological significance, and evidence for a non-unique tectonic setting for Archean crustal growth. Lithos, 123, 21-36. https://doi.org/10.1016/j.lithos.2010.09.015

Moyen, J. -F., & Martin, H. (2012). Forty years of TTG research. Lithos, 148, 312-336. https://doi.org/10.1016/j.lithos.2012.06.010

Möller, C., Andersson, J., Dyck, B., & Lundin, I. A. (2015). Exhumation of an eclogite terrane as a hot migmatitic nappe, Sveconorwegian orogen. Lithos, 226, 147-168. https://doi.org/10.1016/j.lithos.2014.12.013

Möller, C., & Andersson, J. (2018). Metamorphic zoning and behaviour of an underthrusting continental plate. Journal of Metamorphic Geology, 36, 567-589. https://doi.org/10.1111/jmg.12304

Pourteau, A., Doucet, L. S., Blereau, E. R., Volante, S., Johnson, T. E., Collins, W. J., Li, Z. -X., & Champion, D. C. (2020). TTG generation by fluid-fluxed crustal melting: Direct evidence from the Proterozoic Georgetown Inlier, NE Australia. Earth and Planetary Science Letters, 550. https://doi.org/10.1016/j.epsl.2020.116548

Sizova, E., Gerya, T., Stüwe, K., & Brown, M. (2015). Generation of felsic crust in the Archean: A geodynamic modeling perspective. Precambrian Research, 271, 198-224. https://doi.org/10.1016/j.precamres.2015.10.005

Smit, M. A., Musiyachenko, K. A., & Goumans, J. (2024). Archean continental crust formed from mafic cumulates. Nature Communications, 15, 692. https://doi.org/10.1038/s41467-024-44849-4

Smithies, R. H. (2000). The Archean tonalite-trondhjemite-granodiorite (TTG) series is not an analogue of Cenozoic adakite. Earth and Planetary Science Letters, 182, 115-125. https://doi.org/10.1016/S0012-821X(00)00236-3

Tindle, A. G., & Webb, P. C. (1994). Probe-AMPH - A spreadsheet program to classify microprobe-derived amphibole analyses. Computers & Geosciences, 20, 1201-1228. https://doi.org/10.1016/0098-3004(94)90071-X

Wang, X. -D., & Lindh, A. (1996). Temperature-pressure Investigation of the Southern Part of the Southwest Swedish Granulite Region. European Journal of Mineralogy, 8, 51-67. https://doi.org/10.1127/ejm/8/1/0051

Willbold, M., Hegner, E., Stracke, A., & Rocholl, A. Continental geochemical signatures in dacites form Iceland and implications for models of early Archean crust formation. Earth and Planetary Science Letters, 279, 44-52. https://doi.org/10.1016/j.epsl.2008.12.029

Winter, J. D. (2014). Principles of Igneous and Metamorphic Petrology (2nd ed.). Pearson Education Limited.

Wolf, M. B., & Wyllie, P. J. (1991). Dehydration-Melting of Solid Amphibolite at 10 kbar: Textural Development, Liquid Interconnectivity and Applications to the Segregation of Magmas. Mineralogy and Petrology, 44, 151-179. https://doi.org/10.1007/BF01166961

Wolf, M. B., & Wyllie, P. J. (1994). Dehydration-melting of amphibolite at 10 kbar: the effects of temperature and time. Contributions to Mineralogy and Petrology, 115, 369-383. https://doi.org/10.1007/BF00320972

Yardley, B. W. D. (1989). An introduction to metamorphic petrology. Longman Scientific & Technical.

Zhang, C., Holtz, F., Koepke, J., Wolff, P. E., Ma, C., & Bédard, J. H. (2013). Constraints from experimental melting of amphibolite on the depth of formation of garnet-rich restites, and implications for models of Early Archean crustal growth. Precambrian Research, 231, 206-217. https://doi.org/10.1016/j.precamres.2013.03.004

Appendix I. Selected sections on slabs from the garnet amphibolite sample (2A, 3 and 4) and from the melt accumulation vein sample (T1).

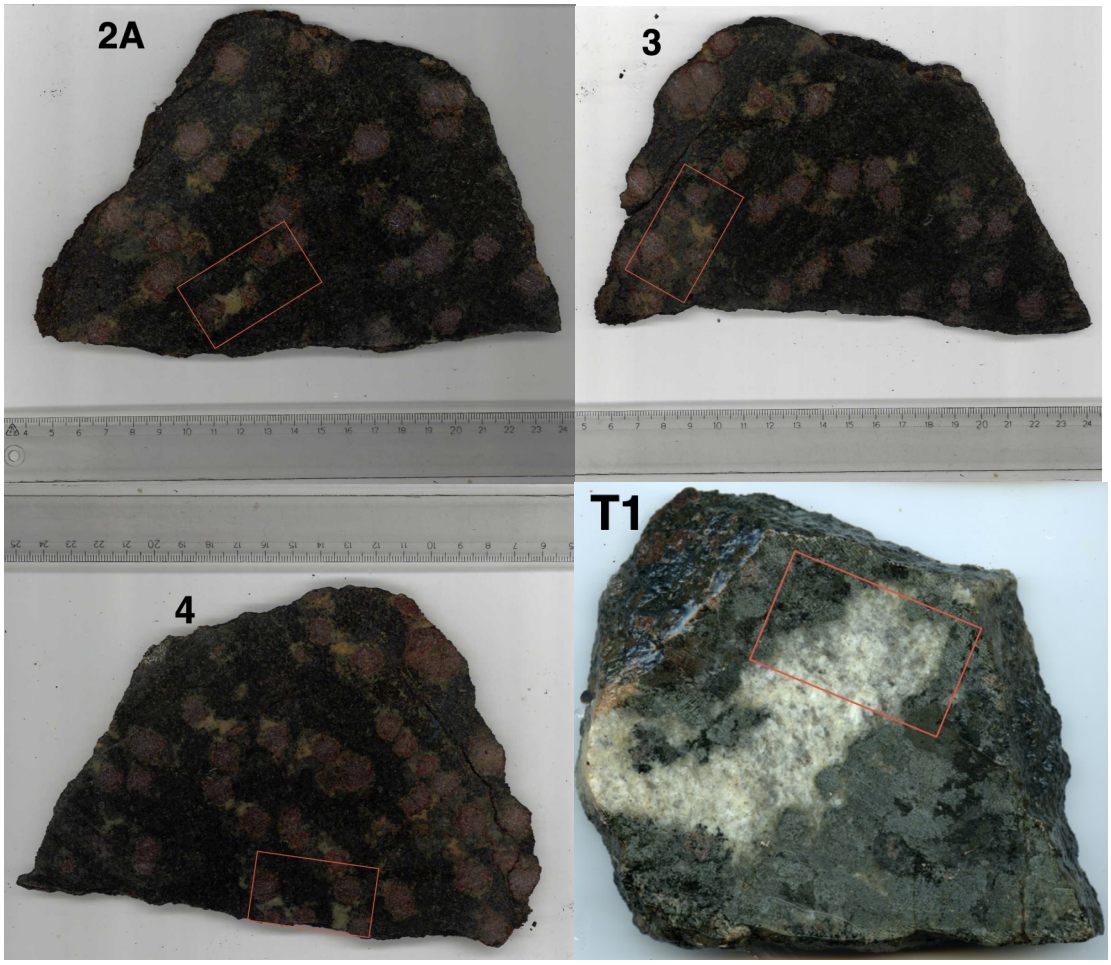

Appendix II. Overview of qz-plag areas in sections of the garnet amphibolite sample and distribution of analyzed 2000x2000 µm areas.

2A (1/3)

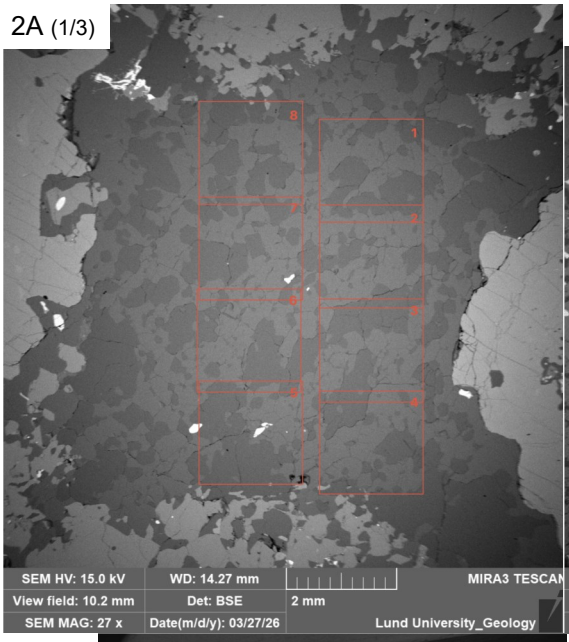

3 (2/3)

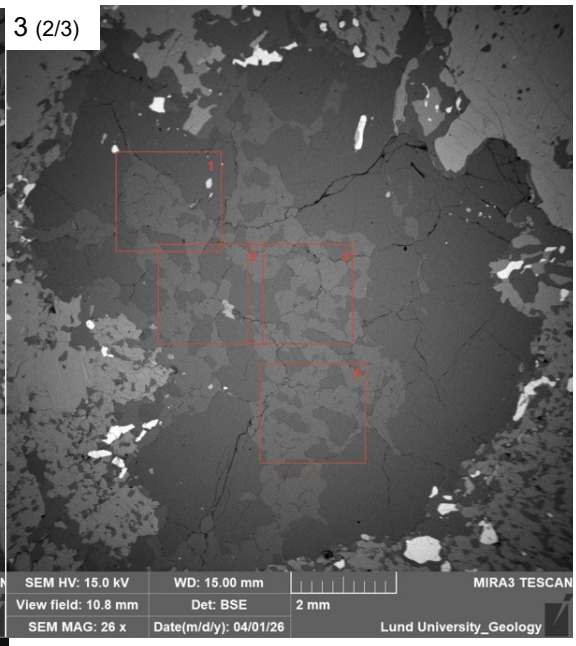

4 (3/5)

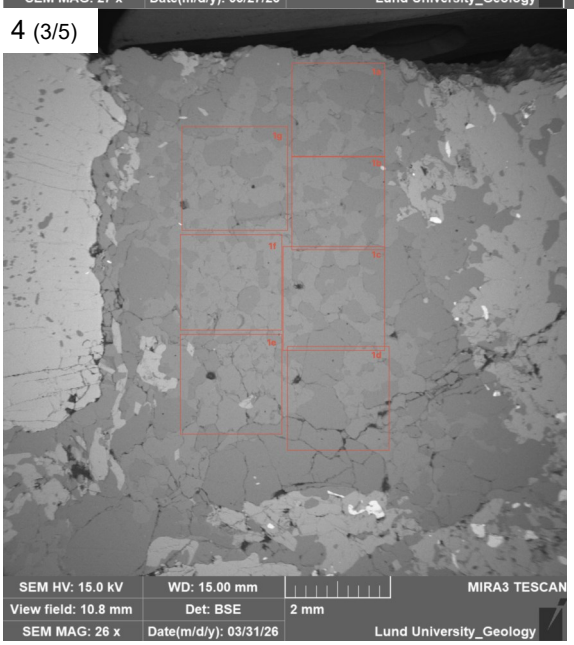

Appendix III. Overview of matrix domains in sections of the garnet amphibolite sample and distribution of analyzed 2000x2000 µm areas.

2A (1/3)

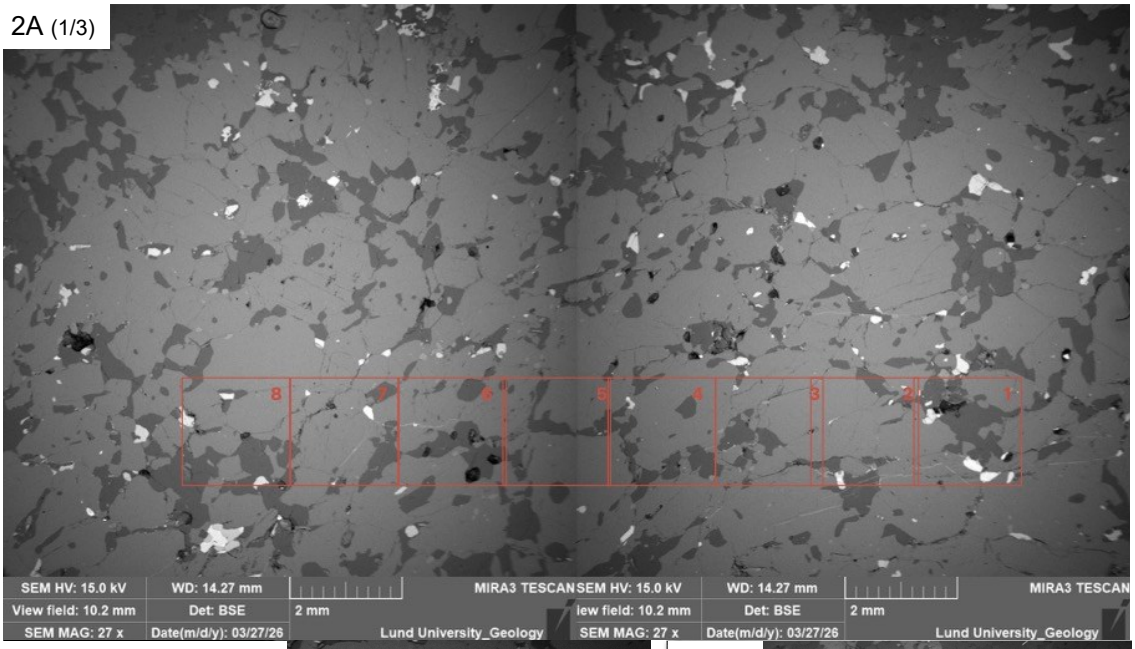

3 (2/3) (hornblende matrix)

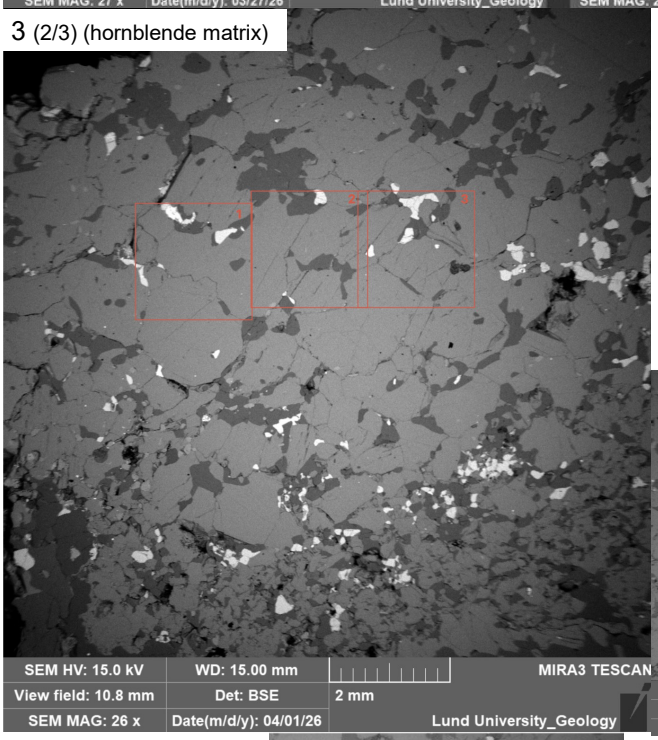

4 (3/5)

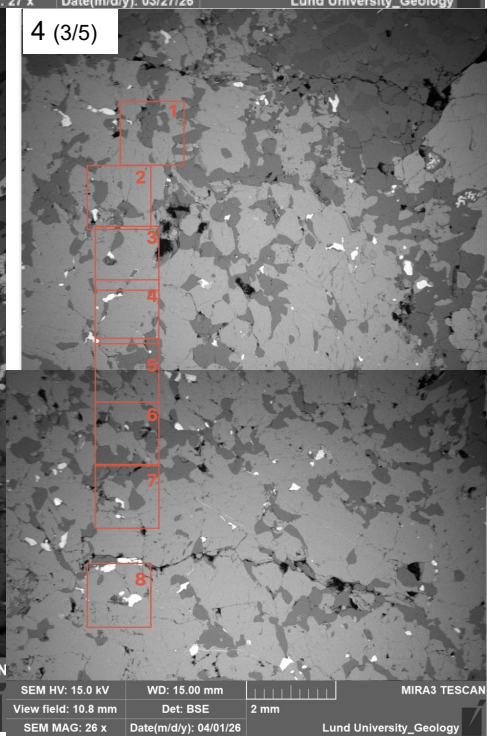

3 (2/3) (pyroxene matrix)

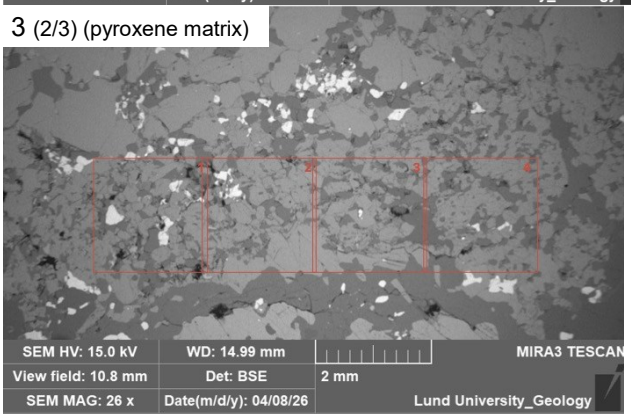

Appendix IV. EDS-analyzed plagioclase in the qz-plag areas of the garnet amphibolite sample (section 2A (1/3), 3 (2/3) and 4 (3/5)).

plag qz-plag area																		
Section	2A (1/3)	2A (1/3)	2A (1/3)	2A (1/3)	2A (1/3)	2A (1/3)	2A (1/3)	2A (1/3)	2A (1/3)	2A (1/3)	2A (1/3)	2A (1/3)	2A (1/3)	2A (1/3)	2A (1/3)	2A (1/3)	2A (1/3)	2A (1/3)
Na2O	7.96	7.87	7.84	7.81	7.97	7.69	7.88	7.9	7.77	7.75	7.81	7.69	7.85	7.75	7.82	7.91	7.81	7.7
MgO	0.03	0.1	0.04	0.04	0.05	0.04	0.03	0.07	0.07	0.05	0.04	0.09	0.26	0.05	0.05	0.06	0.01	0.04
Al2O3	24.22	24.42	24.39	24.48	24.4	24.5	24.43	24.21	24.53	24.44	24.45	24.72	24.1	24.69	24.77	24.46	24.73	24.93
SiO2	61.59	61.5	61.62	61.17	61.43	61.07	61.3	61.54	61.21	61.29	61.25	60.89	61.35	60.85	60.92	61.1	60.94	60.4
P2O5	0	0	0	0	0.03	0	0	0	0.07	0	0	0.02	0	0.01	0	0.03	0	0
S	0	0	0	0	0.02	0	0.01	0.04	0	0.05	0.06	0.04	0	0.03	0.04	0	0.04	0
K2O	0.5	0.55	0.53	0.57	0.5	0.54	0.61	0.52	0.56	0.53	0.54	0.44	0.42	0.38	0.39	0.54	0.42	0.48
CaO	5.54	5.41	5.42	5.66	5.54	5.8	5.5	5.56	5.6	5.74	5.68	5.95	5.45	6.04	5.92	5.69	5.86	6.16
TiO2	0.03	0.05	0.04	0	0.01	0.04	0	0.02	0	0.01	0.09	0	0	0.08	0	0.01	0.01	0.08
V2O5	0	0	0	0.05	0	0	0.05	0	0.02	0.03	0.01	0.04	0.05	0	0.01	0.04	0.03	0
Cr2O3	0	0	0.04	0.09	0	0.05	0	0	0.03	0	0	0.06	0.09	0	0.02	0	0	0.04
MnO	0	0	0	0	0	0.01	0	0.1	0	0.01	0	0	0	0.05	0	0	0	0
FeO	0.11	0.11	0.07	0.11	0.06	0.18	0.12	0.05	0.14	0.06	0.06	0.06	0.41	0.06	0.05	0.15	0.15	0.1
ZrO2	0	0	0	0	0	0.08	0.07	0	0	0.04	0	0	0	0	0.04	0	0	0.08
Total	100	100	100	100	100	100	100	100	100	100	100	100	100	100	100	100	100	100

plag qz-plag area																		
Section	3 (2/3)	3 (2/3)	3 (2/3)	3 (2/3)	3 (2/3)	3 (2/3)	3 (2/3)	3 (2/3)	3 (2/3)	3 (2/3)	3 (2/3)	3 (2/3)	3 (2/3)	3 (2/3)	3 (2/3)	4 (3/5)	4 (3/5)	4 (3/5)
Na2O	8.38	7.65	7.76	7.85	7.57	7.81	7.62	7.6	7.79	7.55	8.58	8.29	7.69	7.71	7.56	8.13	8.22	8.02
MgO	0.13	0.06	0.05	0.05	0.05	0.06	0.03	0.06	0.05	0.1	0.1	0.05	0.05	0.04	0.02	0.05	0.08	0.07
Al2O3	23.58	25.09	24.83	24.81	25.15	24.81	25.19	25.05	24.72	25.05	24.95	24.93	25	25.02	25.17	24.84	24.36	24.85
SiO2	62.33	60.29	60.77	60.8	60.18	60.69	60.37	60.34	60.85	60.4	60.6	60.78	60.37	60.31	60.34	60.81	61.4	60.89
P2O5	0	0	0	0.01	0	0	0.04	0	0	0	0.06	0.01	0	0	0.02	0	0	0
S	0.01	0	0.09	0.07	0	0	0	0	0.01	0.03	0.05	0	0.05	0	0	0.03	0.01	0.03
K2O	0.51	0.46	0.45	0.48	0.43	0.43	0.41	0.42	0.5	0.47	0.44	0.45	0.46	0.45	0.48	0.47	0.47	0.43
CaO	4.74	6.24	5.95	5.81	6.41	5.92	6.19	6.36	5.86	6.24	5.1	5.34	6.24	6.31	6.38	5.57	5.22	5.59
TiO2	0.08	0	0	0.07	0	0.07	0.06	0.01	0.07	0.04	0.01	0.05	0	0	0	0.01	0	0.02
V2O5	0.05	0	0.05	0	0.07	0.04	0	0	0.06	0.06	0.03	0	0.06	0.03	0.03	0	0	0.02
Cr2O3	0	0	0.02	0	0	0	0	0.08	0	0	0	0.02	0	0	0	0.01	0.09	0
MnO	0	0	0	0	0.04	0.03	0	0.01	0	0	0.04	0	0.02	0.03	0	0.01	0	0.02
FeO	0.11	0.2	0.03	0.06	0.1	0.05	0.06	0.08	0.08	0.06	0.04	0.05	0.01	0.11	0	0.09	0.12	0.06
ZrO2	0.08	0.02	0	0	0	0.1	0.04	0	0	0	0	0.03	0.08	0	0	0	0.01	0
Total	100	100	100	100	100	100	100	100	100	100	100	100	100	100	100	100	100	100

plag qz-plag area																		
Section	4 (3/5)	4 (3/5)	4 (3/5)	4 (3/5)	4 (3/5)	4 (3/5)	4 (3/5)	4 (3/5)	4 (3/5)	4 (3/5)	4 (3/5)	4 (3/5)	4 (3/5)	4 (3/5)	4 (3/5)	4 (3/5)	4 (3/5)	4 (3/5)
Na2O	8.15	8.06	7.8	7.75	7.98	5.89	8.34	8.07	7.81	7.97	7.42	7.85	7.68	7.88	8.12	7.59	7.74	7.93
MgO	0.04	0.03	0.06	0.17	0.02	0.05	0.02	0.03	0.07	0.06	0.07	0.06	0.02	0.03	0.08	0.89	0.05	0.05
Al2O3	24.74	25.07	24.68	24.58	24.55	24.68	25.05	24.64	24.8	24.28	24.99	24.59	24.71	24.59	24.1	23.97	25.14	24.74
SiO2	60.7	60.57	61.07	61.02	61.26	60.67	60.6	61.15	60.79	61.53	60.42	61.19	60.94	60.94	61.82	60.57	60.46	61.01
P2O5	0.01	0	0	0	0.03	0.05	0	0.05	0	0.01	0	0.01	0	0	0.01	0	0	0
S	0.02	0.03	0.01	0	0	0	0.04	0	0	0	0	0	0	0	0.02	0	0.02	0
K2O	0.48	0.41	0.41	0.44	0.46	0.57	0.39	0.46	0.4	0.53	0.93	0.47	0.45	0.48	0.55	0.41	0.43	0.42
CaO	5.73	5.64	5.81	5.81	5.65	7.92	5.35	5.5	5.95	5.4	5.85	5.69	5.93	5.75	5.12	5.66	5.86	5.73
TiO2	0	0	0	0.04	0.02	0.05	0.08	0.03	0	0.04	0.21	0.06	0	0	0	0	0.04	0
V2O5	0	0.01	0.02	0	0	0	0.04	0	0	0	0	0.01	0	0.09	0	0	0.02	0.03
Cr2O3	0	0.02	0	0	0	0	0	0.01	0	0	0	0	0	0.1	0.04	0.03	0	0.03
MnO	0	0.02	0	0	0	0.03	0	0.02	0.09	0.02	0.02	0	0.06	0.01	0	0	0.03	0.01
FeO	0.13	0.13	0.15	0.19	0.03	0.08	0.09	0.05	0.07	0.16	0.1	0.07	0.15	0.01	0.13	0.88	0.16	0.01
ZrO2	0	0	0	0	0	0	0	0	0	0	0	0	0.06	0.13	0	0	0.04	0.03
Total	100	100	100	100	100	100	100	100	100	100	100	100	100	100	100	100	100	100

plag qz-plag area													
Section	4 (3/5)	4 (3/5)	4 (3/5)	4 (3/5)	4 (3/5)	4 (3/5)	4 (3/5)	4 (3/5)	4 (3/5)	4 (3/5)	4 (3/5)	4 (3/5)	4 (3/5)
Na2O	7.83	8.25	8.04	7.88	8.04	7.84	8	7.98	7.87	7.89	7.03	7.87	7.7
MgO	0.03	0.06	0.07	0.03	0.09	0.2	0.05	0.05	0.07	0.06	0.11	0.05	0.03
Al2O3	24.84	25.04	25.12	24.69	24.5	24.96	25.25	25.15	25.39	25.1	24.95	25.15	25.07
SiO2	60.74	60.72	60.48	61.02	60.84	60.39	60.33	60.56	60.17	60.75	60.78	60.27	60.58
P2O5	0	0	0.04	0	0	0	0.04	0	0	0.02	0	0	0
S	0	0	0.03	0.01	0.01	0.03	0	0	0	0.04	0.14	0	0.01
K2O	0.48	0.4	0.4	0.45	0.4	0.43	0.34	0.36	0.38	0.46	0.44	0.39	0.38
CaO	5.93	5.36	5.68	5.72	5.94	5.84	5.84	5.76	5.94	5.58	6.4	5.95	5.96
TiO2	0.01	0	0.02	0.04	0	0.01	0	0.01	0.04	0.04	0.01	0	0.02
V2O5	0.03	0	0	0	0.04	0.05	0.05	0.03	0	0	0	0.08	0.07
Cr2O3	0	0	0	0	0.05	0	0	0	0	0	0.03	0.05	0
MnO	0.04	0.02	0.04	0	0.02	0	0.05	0	0	0.01	0	0.02	0
FeO	0.02	0.04	0.08	0.05	0.03	0.15	0.05	0.09	0.16	0.05	0.12	0.05	0.07
ZrO2	0.06	0.11	0	0.11	0.04	0.1	0	0	0	0	0	0.12	0.11
Total	100	100	100	100	100	100	100	100	100	100	100	100	100

Appendix V. EDS-analyzed plagioclase in the melt accumulation vein sample (section T1 (1/2)).

plag qz-plag area																				
Section	T1 (1/2)	T1 (1/2)	T1 (1/2)	T1 (1/2)	T1 (1/2)	T1 (1/2)	T1 (1/2)	T1 (1/2)	T1 (1/2)	T1 (1/2)	T1 (1/2)	T1 (1/2)	T1 (1/2)	T1 (1/2)	T1 (1/2)	T1 (1/2)	T1 (1/2)	T1 (1/2)	T1 (1/2)	T1 (1/2)
Na2O	8.51	8.31	8.52	8.58	8.31	8.33	8.31	8.21	8.37	8.55	10.07	8.4	8.44	8.46	8.3	8.22	8.57	8.49	8.33	8.43
MgO	0.08	0.05	0.05	0.06	0.03	0.06	0.07	0.07	0.04	0.07	0.09	0.04	0.04	0.07	0.06	0.03	0.04	0.06	0.05	0
Al2O3	23.72	23.98	23.52	23.64	24.19	23.98	23.95	24.25	23.88	23.73	22.24	23.98	23.86	23.95	24.07	24.22	23.77	23.86	24.28	23.9
SiO2	62.43	62.18	62.68	62.5	61.8	61.89	61.91	61.66	62.12	62.13	65.35	61.81	62.24	62.17	61.99	61.75	62.35	62.27	61.68	62.22
P2O5	0	0	0	0	0	0	0	0	0	0.02	0	0.04	0	0	0	0.02	0	0	0	0
S	0.02	0	0.04	0	0.04	0	0	0	0	0.03	0	0.03	0	0	0.05	0	0.01	0	0	0.04
K2O	0.37	0.4	0.6	0.33	0.34	0.38	0.37	0.32	0.49	0.37	0.96	0.4	0.37	0.28	0.43	0.4	0.39	0.3	0.33	0.33
CaO	4.67	4.99	4.45	4.72	5.11	5.09	5.15	5.3	4.88	4.77	1.19	5.01	4.89	4.94	4.94	5.22	4.65	4.81	5.16	4.96
TiO2	0.06	0	0.03	0	0	0.03	0.05	0.01	0.02	0.02	0	0.07	0	0.01	0.03	0	0	0	0	0
V2O5	0	0	0	0	0	0.02	0	0	0.04	0.05	0	0	0.04	0.01	0.03	0	0.01	0.04	0.06	0.04
Cr2O3	0	0	0	0	0	0	0	0	0	0.03	0	0.01	0	0	0.01	0.03	0.02	0.03	0	0
MnO	0	0	0.02	0.04	0.04	0	0	0	0	0.04	0	0.02	0	0	0	0	0.06	0	0.03	0
FeO	0.13	0.08	0.09	0.12	0.1	0.17	0.18	0.14	0.18	0.16	0.09	0.2	0.04	0.09	0.1	0.11	0	0.14	0.05	0.08
ZrO2	0.01	0	0.01	0	0.03	0.05	0	0.03	0	0.03	0.02	0	0.07	0	0	0	0.14	0	0.03	0
Total	100	100	100	100	100	100	100	100	100	100	100	100	100	100	100	100	100	100	100	100

plag qz-plag area																				
Section	T1 (1/2)	T1 (1/2)	T1 (1/2)	T1 (1/2)	T1 (1/2)	T1 (1/2)	T1 (1/2)	T1 (1/2)	T1 (1/2)	T1 (1/2)	T1 (1/2)	T1 (1/2)	T1 (1/2)	T1 (1/2)	T1 (1/2)	T1 (1/2)	T1 (1/2)	T1 (1/2)	T1 (1/2)	T1 (1/2)
Na2O	9.18	8.21	8.16	7.73	8.87	8.47	8.38	8.43	8.34	8.32	8.48	8.45	4.86	8.41	8.33	6.06	8.44	8.45	7.21	
MgO	0.07	0.04	0.05	0.02	0.06	0.07	0.06	0.03	1.2	0.05	0.02	0.04	0.14	0.05	0.05	0.08	0.06	0.07	0.09	
Al2O3	23.61	24.04	24.33	23.94	23.36	24.61	23.82	23.81	23.15	23.98	23.82	23.97	29.71	23.62	23.86	28.04	23.98	24.07	23.69	
SiO2	63.99	61.96	61.52	62.46	63.06	62.82	62.22	62.57	61.59	62.12	62.3	62.15	58.3	62.31	62.36	59.62	61.95	61.89	59.83	
P2O5	0.01	0	0.02	0.02	0	0	0	0.02	0.03	0.04	0	0.02	0.01	0	0	0	0	0	0	
S	0	0.03	0	0.04	0	0.03	0	0.03	0	0	0.07	0.01	0	0.01	0.05	0.01	0	0	0	
K2O	1.85	0.35	0.27	0.37	0.31	2.33	0.43	0.35	0.44	0.4	0.38	0.34	5.49	0.41	0.35	4.83	0.25	0.35	0.21	
CaO	1.12	5.22	5.43	5.36	4.26	1.15	4.81	4.72	4.26	4.92	4.74	4.84	0.93	4.88	4.93	0.89	4.98	5.03	8.85	
TiO2	0	0	0.06	0	0	0.05	0.02	0.05	0	0.03	0.02	0.04	0.01	0	0.05	0.08	0.05	0.03	0.04	
V2O5	0	0.02	0	0.03	0	0.1	0	0	0	0	0.05	0	0	0.07	0.02	0	0.07	0.02	0	
Cr2O3	0	0	0.02	0.01	0	0.01	0.13	0	0.04	0	0	0	0	0	0	0	0	0.06	0.01	
MnO	0.01	0.03	0	0.02	0	0.11	0	0	0.05	0	0	0.04	0	0.02	0	0.03	0.02	0	0	
FeO	0.16	0.08	0.12	0	0.07	0.24	0.06	0	0.89	0.13	0.11	0.07	0.5	0.21	0	0.29	0.09	0.03	0.08	
ZrO2	0	0	0.02	0	0.02	0	0.07	0	0	0	0	0.04	0.04	0	0	0.06	0.1	0.01	0	
Total	100	100	100	100	100	100	100	100	100	100	100	100	100	100	100	100	100	100	100	

Appendix VI. EDS-analyzed plagioclase in the amphibolite matrix of the garnet amphibolite sample (section 2A (1/3), 3 (2/3) and 4 (3/5)).

plag hbl matrix																				
Section	2A (1/3)	2A (1/3)	2A (1/3)	2A (1/3)	2A (1/3)	2A (1/3)	2A (1/3)	2A (1/3)	2A (1/3)	2A (1/3)	2A (1/3)	2A (1/3)	2A (1/3)	2A (1/3)	2A (1/3)	2A (1/3)	2A (1/3)	2A (1/3)	2A (1/3)	2A (1/3)
Na2O	7.01	7.06	6.9	6.99	6.9	7.28	7.17	7.19	7.34	7.28	7.51	7.38	7.17	7.41	7.31	7.55	7.19	7.42	7.62	
MgO	0.04	0.04	0.06	0.09	0.02	0.06	0.06	0.09	0.05	0.06	0.06	0.05	0.06	0.07	0.04	0.15	0.07	0.09	0.09	
Al2O3	25.98	25.98	25.98	26.06	26.19	25.71	25.89	25.91	25.54	25.63	25.21	25.45	25.77	25.47	25.53	25.07	25.65	25.16	24.96	
SiO2	59.14	59.18	59.29	58.96	58.72	59.59	59.16	59.18	59.69	59.67	60	59.96	59.45	59.95	59.91	60.16	59.93	60.28	60.7	
P2O5	0.03	0	0.01	0	0.05	0.05	0	0	0	0.01	0	0	0	0	0.01	0.07	0.02	0.01	0.08	
S	0.01	0.03	0	0	0	0	0.02	0.04	0.07	0.02	0	0.02	0	0	0	0.01	0	0	0.01	
K2O	0.26	0.24	0.23	0.27	0.3	0.27	0.2	0.18	0.28	0.26	0.25	0.26	0.34	0.29	0.28	0.27	0.25	0.4	0.24	
CaO	7.32	7.38	7.33	7.43	7.66	6.94	7.27	7.17	6.78	6.94	6.65	6.74	7.09	6.66	6.77	6.37	6.85	6.53	6.23	
TiO2	0.04	0.03	0.04	0.04	0	0	0	0.04	0.03	0	0	0.05	0	0.02	0.01	0.02	0	0	0.03	
V2O5	0.04	0	0	0	0	0.03	0	0	0	0	0.06	0	0	0	0	0	0.04	0.01	0	
Cr2O3	0.01	0	0.04	0	0.05	0	0.1	0.07	0	0.03	0	0	0	0	0	0	0.01	0.06	0	
MnO	0.03	0.02	0	0.05	0.02	0.06	0	0	0	0	0	0	0	0.02	0	0.02	0	0.03	0	
FeO	0.1	0.04	0.1	0.04	0.09	0.02	0.12	0.08	0.22	0.09	0.17	0.02	0.07	0.11	0.14	0.28	0	0	0.04	
ZrO2	0	0.01	0	0.07	0	0	0	0.05	0	0	0.09	0.07	0.04	0	0	0.03	0	0	0	
Total	100	100	100	100	100	100	100	100	100	100	100	100	100	100	100	100	100	100	100	

plag hbl matrix																				
Section	3 (2/3)	3 (2/3)	3 (2/3)	3 (2/3)	3 (2/3)	3 (2/3)	3 (2/3)	3 (2/3)	4 (3/5)	4 (3/5)	4 (3/5)	4 (3/5)	4 (3/5)	4 (3/5)	4 (3/5)	4 (3/5)	4 (3/5)	4 (3/5)	4 (3/5)	4 (3/5)
Na2O	7.38	7.14	7.21	7.18	7.39	7.28	7.48	7.74	7.51	7.55	7.41	7.72	7.34	7.27	7.43	7.19	7.21	7.24	7.13	
MgO	0.05	0.19	0.08	0.07	0.04	0.04	0.06	0.05	0.06	0.08	0.06	0.09	0.05	0.09	0.03	0.03	0.08	0.08	0.04	
Al2O3	25.77	26.02	25.92	26.11	25.76	26.04	25.6	25.5	25.63	25.31	25.56	25.2	25.81	25.71	25.52	26.07	25.95	25.82	26.08	
SiO2	59.19	58.08	58.87	58.6	59.32	58.98	59.67	59.72	59.8	59.99	59.63	60.27	59.25	59.58	59.67	58.86	59.21	59.29	59.01	
P2O5	0.02	0.04	0	0.03	0.03	0	0	0.01	0.01	0.05	0	0	0	0	0.02	0	0	0.06	0	
S	0	0	0.04	0.09	0.01	0.04	0.01	0.04	0	0.01	0.07	0.02	0.12	0.05	0	0.09	0	0	0.02	
K2O	0.22	0.65	0.38	0.2	0.26	0.25	0.17	0.25	0.34	0.35	0.32	0.31	0.34	0.35	0.33	0.17	0.23	0.24	0.13	
CaO	7.03	6.37	7.15	7.38	6.98	7.08	6.77	6.48	6.52	6.37	6.71	6.13	6.88	6.85	6.76	7.26	7.08	7.1	7.4	
TiO2	0.03	0	0.07	0	0.03	0.06	0.03	0	0.04	0.03	0.01	0.02	0.04	0	0.01	0	0	0.03	0	
V2O5	0	0	0.04	0.05	0.06	0	0.03	0.03	0.01	0.06	0	0.06	0	0.04	0	0.07	0.07	0	0.01	
Cr2O3	0.06	0	0	0	0.03	0.01	0.02	0.05	0	0	0.02	0	0	0	0	0.03	0	0	0	
MnO	0.01	0.08	0.02	0.06	0	0.01	0	0.03	0	0.04	0.06	0	0.02	0	0	0	0	0.01	0.03	
FeO	0.23	1.43	0.22	0.24	0.1	0.22	0.14	0.1	0.08	0.15	0.12	0.14	0.15	0.06	0.21	0.23	0.15	0.12	0.16	
ZrO2	0	0	0	0	0	0	0	0	0	0	0.02	0.04	0	0	0.01	0	0.01	0	0	
Total	100	100	100	100	100	100	100	100	100	100	100	100	100	100	100	100	100	100	100	

plag hbl matrix										
Section	4 (3/5)	4 (3/5)	4 (3/5)	4 (3/5)	4 (3/5)	4 (3/5)	4 (3/5)	4 (3/5)	4 (3/5)	4 (3/5)
Na2O	7.48	7.43	7.26	7.16	7.35	7.21	7.28	7.21	7.37	7.38
MgO	0.05	0.08	0.09	0.07	0.05	0.06	0.08	0.07	0.03	0.06
Al2O3	25.67	25.69	25.68	26.06	25.55	25.83	25.86	25.91	25.58	25.64
SiO2	59.55	59.31	59.53	58.98	59.69	59.17	59.35	59.28	59.84	59.39
P2O5	0	0	0.02	0	0.04	0.02	0.06	0	0	0
S	0	0.01	0.02	0	0	0	0	0.06	0	0.01
K2O	0.29	0.33	0.28	0.25	0.3	0.28	0.25	0.22	0.31	0.25
CaO	6.77	6.98	6.9	7.24	6.78	7.29	7.02	7.07	6.72	6.87
TiO2	0	0	0.02	0	0.1	0.07	0	0	0.02	0.08
V2O5	0	0	0	0	0	0	0	0.02	0	0
Cr2O3	0.01	0.07	0.01	0.02	0	0	0	0.02	0.06	0
MnO	0.05	0.02	0	0.04	0	0	0	0.01	0	0.05
FeO	0.13	0.06	0.2	0.15	0.05	0.08	0.1	0.12	0.05	0.28
ZrO2	0	0.03	0	0.01	0.1	0	0	0.01	0.03	0
Total	100	100	100	100	100	100	100	100	100	100

plag px matrix								
Section	3 (2/3)	3 (2/3)	3 (2/3)	3 (2/3)	3 (2/3)	3 (2/3)	3 (2/3)	3 (2/3)
Na2O	7.96	7.88	7.68	7.73	7.73	7.74	7.69	7.73
MgO	0.05	0.06	0.01	0.06	0	0.02	0.02	0.01
Al2O3	24.77	24.93	25.21	25.06	25.15	25	25.07	25.09
SiO2	60.85	60.41	60.11	60.46	60.12	60.45	60.22	60.5
P2O5	0.04	0.04	0	0.02	0	0	0	0
S	0	0.01	0	0	0	0	0.05	0
K2O	0.27	0.3	0.35	0.39	0.36	0.49	0.43	0.4
CaO	5.97	6.18	6.37	6.16	6.43	6.16	6.27	6.16
TiO2	0.02	0.02	0.02	0	0.01	0	0	0
V2O5	0	0	0.01	0.01	0	0	0	0
Cr2O3	0	0.01	0.06	0	0	0	0	0.05
MnO	0.01	0	0	0.02	0	0.03	0.02	0
FeO	0.06	0.15	0.12	0.09	0.2	0.09	0.18	0.07
ZrO2	0	0	0.07	0	0	0.02	0.04	0
Total	100	100	100	100	100	100	100	100

Appendix VII. EDS-analyzed amphibole in the amphibolite matrix of the garnet amphibolite and melt accumulation vein sample (section 2A (1/3), 3 (2/3), 4 (3/5) and T1 (1/2)).

hbl																		
Sample	2A (1/3)	2A (1/3)	2A (1/3)	2A (1/3)	2A (1/3)	2A (1/3)	2A (1/3)	2A (1/3)	2A (1/3)	2A (1/3)	2A (1/3)	2A (1/3)	2A (1/3)	2A (1/3)	2A (1/3)	2A (1/3)	3 (2/3)	3 (2/3)
Na2O	2	1.94	1.96	1.94	1.99	1.94	2.04	2.09	1.88	1.97	2	1.99	2.05	1.95	1.96	2	2.07	2.11
MgO	10.15	10.12	10.32	10.21	9.98	9.9	10.01	9.88	10.31	10.25	10.37	10.56	10.35	10.42	10.43	10.2	10.45	10.18
Al2O3	12.88	12.83	12.58	13.06	12.67	13.02	12.92	12.99	12.69	12.71	12.62	12.3	12.61	12.36	12.46	12.71	12.91	12.89
SiO2	42.28	42.44	42.59	42.51	42.47	42.24	42.1	41.96	42.69	42.58	42.73	42.99	42.48	42.66	42.84	42.58	42.91	42.6
P2O5	0	0	0.02	0	0	0	0.06	0	0.03	0.02	0	0	0	0	0	0	0	0
S	0	0	0.07	0	0.03	0.08	0.05	0.02	0.03	0.05	0.05	0	0.03	0.09	0.08	0.06	0.04	0.02
K2O	1.26	1.29	1.25	1.25	1.27	1.27	1.34	1.31	1.24	1.24	1.2	1.19	1.3	1.24	1.23	1.25	1.23	1.22
CaO	11.35	11.33	11.22	11.28	11.28	11.3	11.31	11.39	11.34	11.36	11.1	11.22	11.34	11.31	11.24	11.14	10.93	11.12
TiO2	2.36	2.44	2.39	2.1	2.51	2.55	2.65	2.44	2.42	2.38	2.32	2.46	2.62	2.69	2.34	2.45	2.13	2.3
V2O5	0.17	0.2	0.1	0.14	0.2	0.08	0.18	0.22	0.13	0.18	0.18	0.08	0.1	0.18	0.13	0.18	0.12	0.18
Cr2O3	0	0	0.08	0	0	0.08	0.07	0.11	0	0.01	0.05	0	0.01	0	0.07	0	0.09	0
MnO	0.03	0.15	0.08	0.11	0.06	0.03	0.07	0	0.07	0.06	0.04	0.05	0.08	0.1	0	0.1	0.07	0.05
FeO	17.5	17.2	17.34	17.32	17.51	17.36	17.18	17.4	17.17	17.19	17.34	17.06	16.96	16.91	17.24	17.29	17.05	17.35
ZrO2	0.01	0.06	0	0.08	0.04	0.12	0.02	0.18	0	0	0.01	0.09	0.06	0.1	0	0.05	0	0
Total	100	100	100	100	100	100	100	100	100	100	100	100	100	100	100	100	100	100
hbl																		
Sample	3 (2/3)	3 (2/3)	3 (2/3)	3 (2/3)	3 (2/3)	3 (2/3)	3 (2/3)	4 (3/5)	4 (3/5)	4 (3/5)	4 (3/5)	4 (3/5)	4 (3/5)	4 (3/5)	4 (3/5)	4 (3/5)	4 (3/5)	4 (3/5)
Na2O	1.97	2.03	1.78	2.04	1.99	1.86	1.77	1.91	1.88	1.88	1.97	1.97	1.96	2.04	2.13	2.09	2	2.04
MgO	10.17	10.22	10.72	10.25	9.64	9.5	9.83	10.09	9.96	10.35	10.1	9.98	10	10.02	10.01	9.93	10.04	9.92
Al2O3	12.64	12.69	11.81	12.36	11.89	12	11.19	12.11	11.92	11.64	12.47	12.29	12.41	12.88	12.71	12.9	12.94	12.81
SiO2	42.81	42.84	43.98	42.83	42.74	43.27	43.69	42.88	43.2	43.7	43.15	43.21	43.02	42.2	42.6	42.39	42.67	42.53
P2O5	0	0	0	0	0	0	0	0	0.02	0	0	0	0.09	0	0.03	0	0.13	0.04
S	0.09	0.01	0.03	0.06	0.08	0	0.11	0.12	0.07	0.06	0	0.01	0.03	0.09	0	0.01	0.07	0
K2O	1.22	1.27	1.13	1.13	1.19	1.21	1.12	1.2	1.18	1.14	1.18	1.22	1.19	1.22	1.18	1.19	1.18	1.23
CaO	11.1	11.05	11.34	11.03	11.14	11.07	11.18	11.29	11.22	11.31	11.09	11.18	11.1	11.14	11.07	11.05	11.14	11.08
TiO2	2.37	2.56	2.17	2.43	2.28	2.21	2.1	2.03	2.24	2.43	2.11	2.33	2.36	2.24	2.41	2.45	2.15	2.35
V2O5	0.21	0.1	0.16	0.15	0.3	0.31	0.35	0.13	0.12	0.06	0.12	0.19	0.13	0.17	0.1	0.25	0.16	0.15
Cr2O3	0.01	0.11	0.02	0.06	0.02	0.05	0	0	0	0	0.02	0	0	0.03	0.1	0.06	0.03	0
MnO	0.09	0.13	0.12	0.04	0	0.04	0.1	0.08	0.01	0.01	0.07	0.02	0.05	0	0.09	0	0.02	0.09
FeO	17.31	16.97	16.68	17.63	18.64	18.49	18.52	18.09	18.18	17.41	17.71	17.6	17.65	17.98	17.56	17.61	17.46	17.76
ZrO2	0	0.02	0.07	0	0.08	0	0.03	0.08	0	0	0.01	0	0	0	0	0.06	0	0
Total	100	100	100	100	100	100	100	100	100	100	100	100	100	100	100	100	100	100
hbl																		
Sample	4 (3/5)	4 (3/5)	4 (3/5)	4 (3/5)	4 (3/5)	4 (3/5)	4 (3/5)	4 (3/5)	4 (3/5)	4 (3/5)	4 (3/5)	4 (3/5)	T1 (1/2)	T1 (1/2)	T1 (1/2)	T1 (1/2)	T1 (1/2)	T1 (1/2)
Na2O	2.02	2.05	1.99	2.02	1.99	2.11	1.95	1.87	2.04	2.04	2.03	1.96	2.05	2	1.64	2	1.59	1.75
MgO	9.9	10.17	9.98	9.92	10.26	9.96	10.09	10.31	10	10.06	9.91	9.98	8.15	7.89	8.27	8.24	7.92	8.56
Al2O3	12.87	12.71	13.02	12.83	12.69	12.58	12.62	12.41	12.68	12.68	12.73	12.31	11.36	11.52	11.84	13.69	12.02	12.93
SiO2	42.39	42.55	42.65	42.68	42.76	42.79	42.83	43.35	42.54	42.45	42.51	43.03	42.97	43.1	42.5	41.42	40.99	42.11
P2O5	0.02	0.04	0.02	0.04	0	0	0	0.02	0.03	0	0	0.01	0	0	0.05	0.04	0	0.12
S	0.1	0.03	0	0.08	0	0.06	0.01	0	0.02	0.07	0	0.02	0.02	0.05	0.02	0.05	0.05	0.1
K2O	1.23	1.18	1.19	1.21	1.19	1.19	1.19	1.21	1.19	1.19	1.21	1.19	0.82	0.79	1.14	1.14	1.15	1.12
CaO	11.12	11.16	11.16	11.1	11.13	11.15	11.34	11.27	11.26	11.16	11.12	11.17	11.03	11.07	11.34	11.3	12.04	11.13
TiO2	2.53	2.4	2.23	2.34	2.38	2.41	2.42	2.11	2.29	2.31	2.31	2.19	2.08	2.06	1.46	1.87	1.93	1.74
V2O5	0.15	0.07	0.12	0.11	0.23	0.21	0.1	0.17	0.19	0.13	0.18	0.11	0.21	0.21	0.13	0.07	0.1	0.11
Cr2O3	0	0.08	0	0.08	0	0.03	0	0.06	0	0.02	0.03	0	0	0.07	0	0	0	0.06
MnO	0	0.02	0.04	0	0.04	0.11	0.09	0.05	0	0.09	0	0.06	0.1	0.17	0.11	0.19	0.3	0.2
FeO	17.66	17.54	17.61	17.57	17.22	17.39	17.34	17.17	17.78	17.78	17.98	17.97	21.12	21.06	21.48	20	21.89	20.08
ZrO2	0.02	0	0	0	0.11	0.01	0.02	0.01	0	0	0	0	0.09	0	0.01	0	0.02	0
Total	100	100	100	100	100	100	100	100	100	100	100	100	100	100	100	100	100	100

Appendix VIII. Amphibole calculation scheme calculated in probe-Amph (Tindle and Webb, 1994), based on data in appendix VII.

Amphibole calculation scheme - hbl matrix section 2A (1/3), 3 (2/3), 4 (3/5)																								
Sample no	hbl 1	hbl 2	hbl 3	hbl 4	hbl 5	hbl 6	hbl 7	hbl 8	hbl 9	hbl 10	hbl 11	hbl 12	hbl 13	hbl 14	hbl 15	hbl 16	hbl 17	hbl 18	hbl 19	hbl 20	hbl 21	hbl 22	hbl 23
Amphibole group	Ca	Ca	Ca	Ca	Ca	Ca	Ca	Ca	Ca	Ca	Ca	Ca	Ca	Ca	Ca	Ca	Ca	Ca	Ca	Ca	Ca	Ca	Ca
(Ca+Na) (B)	2	2	2	2	2	2	2	2	2	2	2	2	2	2	2	2	2	2	2	2	2	2	2
Na (B)	0.224	0.227	0.249	0.24	0.232	0.229	0.225	0.207	0.230	0.223	0.270	0.252	0.225	0.230	0.247	0.260	0.303	0.265	0.267	0.277	0.237	0.280	0.231
(Na+K) (A)	0.577	0.563	0.537	0.54	0.57	0.558	0.605	0.634	0.531	0.565	0.516	0.530	0.597	0.553	0.535	0.538	0.506	0.558	0.516	0.531	0.473	0.505	0.534
Mg/(Mg+Fe2)	0.584	0.582	0.598	0.6	0.57	0.57	0.57	0.560	0.593	0.585	0.606	0.604	0.585	0.591	0.599	0.592	0.619	0.590	0.591	0.591	0.604	0.598	0.581
Fe3/(Fe3+Alvi)	0.591	0.56	0.625	0.59	0.557	0.54	0.534	0.514	0.584	0.563	0.632	0.613	0.556	0.582	0.609	0.597	0.615	0.581	0.587	0.564	0.555	0.648	0.638
Sum of S2	13	13	13	13	13	13	13	13	13	13	13	13	13	13	13	13	13	13	13	13	13	13	13

Amphibole calculation scheme - hbl matrix section 2A (1/3), 3 (2/3), 4 (3/5)																							
Sample no	hbl 24	hbl 25	hbl 26	hbl 27	hbl 28	hbl 29	hbl 30	hbl 31	hbl 32	hbl 33	hbl 34	hbl 35	hbl 36	hbl 37	hbl 38	hbl 39	hbl 40	hbl 41	hbl 42	hbl 43	hbl 44	hbl 45	
Amphibole group	Ca	Ca	Ca	Ca	Ca	Ca	Ca	Ca	Ca	Ca	Ca	Ca	Ca	Ca	Ca	Ca	Ca	Ca	Ca	Ca	Ca	Ca	
(Ca+Na) (B)	2	2	2	2	2	2	2	2	2	2	2	2	2	2	2	2	2	2	2	2	2	2	
Na (B)	0.244	0.235	0.272	0.252	0.265	0.258	0.271	0.271	0.259	0.268	0.260	0.258	0.260	0.265	0.263	0.254	0.228	0.244	0.238	0.255	0.261	0.255	
(Na+K) (A)	0.508	0.508	0.503	0.533	0.510	0.547	0.551	0.543	0.526	0.538	0.542	0.540	0.523	0.532	0.520	0.566	0.545	0.508	0.562	0.543	0.538	0.521	
Mg/(Mg+Fe2)	0.568	0.576	0.587	0.565	0.576	0.590	0.581	0.579	0.586	0.580	0.574	0.590	0.584	0.575	0.595	0.568	0.575	0.589	0.574	0.587	0.577	0.575	
Fe3/(Fe3+Alvi)	0.611	0.561	0.598	0.531	0.576	0.644	0.591	0.586	0.569	0.597	0.578	0.614	0.575	0.560	0.588	0.531	0.542	0.551	0.584	0.628	0.611	0.600	
Sum of S2	13	13	13	13	13	13	13	13	13	13	13	13	13	13	13	13	13	13	13	13	13	13	

Amphibole calculation scheme - px matrix section 3 (2/3)					
Sample no	hbl 1	hbl 2	hbl 3		
Amphibole group	Ca	Ca	Ca		
(Ca+Na) (B)	2	2	2		
Na (B)	0.246	0.263	0.244		
(Na+K) (A)	0.545	0.491	0.468		
Mg/(Mg+Fe2)	0.551	0.545	0.558		
Fe3/(Fe3+Alvi)	0.625	0.568	0.628		
Sum of S2	13	13	13		

Amphibole calculation scheme - matrix section T1 (1/2)						
Sample no	hbl 1	hbl 2	hbl 3	hbl 4	hbl 5	hbl 6
Amphibole group	Ca	Ca	Ca	Ca	Ca	Ca
(Ca+Na) (B)	2	2	2	2	2	2
Na (B)	0.251	0.244	0.204	0.214	0.072	0.247
(Na+K) (A)	0.493	0.479	0.481	0.572	0.608	0.462
Mg/(Mg+Fe2)	0.471	0.455	0.491	0.496	0.459	0.525
Fe3/(Fe3+Alvi)	0.633	0.572	0.690	0.562	0.730	0.642
Sum of S2	13	13	13	13	13	13

Appendix IX. EDS-analyzed garnet in the garnet amphibolite and melt accumulation vein sample (section 2A (1/3), 3 (2/3), 4 (3/5) and T1 (1/2)).

gt Section	2A (1/3)	2A (1/3)	2A (1/3)	3 (2/3)	3 (2/3)	3 (2/3)	3 (2/3)	4 (3/5)	4 (3/5)	4 (3/5)	4 (3/5)	T1 (1/2)	T1 (1/2)	T1 (1/2)
Na2O	0.01	0.06	0.02	0.02	0	0.06	0	0.04	0.05	0.02	0.05	0.01	0	0.02
MgO	2.3	2.24	3.23	2.44	3.42	3.25	3.56	4.16	3.58	2.87	2.67	3.4	3.24	3.25
Al2O3	21.04	21.23	20.32	21.51	21.67	21.63	21.54	21.5	21.12	21.6	21.69	21.36	21.04	21.17
SiO2	37.24	37.32	37.59	37.91	38.25	37.84	38.44	38.35	38.04	38.51	38.3	38.11	37.81	37.98
P2O5	0.02	0	0.01	0.1	0	0.02	0	0.02	0.03	0	0.14	0	0.05	0.01
S	0	0	0.03	0.03	0.02	0	0.05	0	0	0	0	0	0.02	0
K2O	0.02	0.01	0.01	0.03	0	0.02	0.01	0.03	0.05	0.03	0	0.01	0	0.01
CaO	10.17	10.3	12.93	11	9.46	8.7	11.65	9.42	12.15	12.43	11.97	11.06	10.88	9.83
TiO2	0.06	0.07	1.83	0.09	0.08	0.12	0	0.07	0.23	0.11	0.06	0.08	0.04	0.05
V2O5	0.14	0.06	0.07	0.04	0	0.07	0.08	0.01	0.04	0.01	0.07	0.04	0.09	0.08
Cr2O3	0.03	0	0	0.01	0.02	0.06	0	0.07	0	0.03	0	0.03	0.02	0.01
MnO	3.01	2.56	0.33	0.99	1.56	1.66	0.31	0.34	0.29	0.61	0.91	0.68	0.59	1.08
FeO	25.95	26.16	23.61	25.82	25.54	26.58	24.36	25.98	24.38	23.74	24.13	25.22	26.17	26.47
ZrO2	0	0	0	0.01	0	0	0	0	0.02	0.03	0	0	0.04	0.04
Total	100	100	100	100	100	100	100	100	100	100	100	100	100	100

Appendix X. Harker diagram with SiO_2 plotted against CaO, of the qz-plag area, matrix domains and the dominating minerals for the different sections. The mean values of the qz-plag areas and matrix domains are shown as larger dots. Plotted in GCDkit (Janousek et al., 2006). Abbreviations: wr: whole rock, hbl: hornblende, px: pyroxene, gt: garnet, plag: plagioclase, qz: quartz,

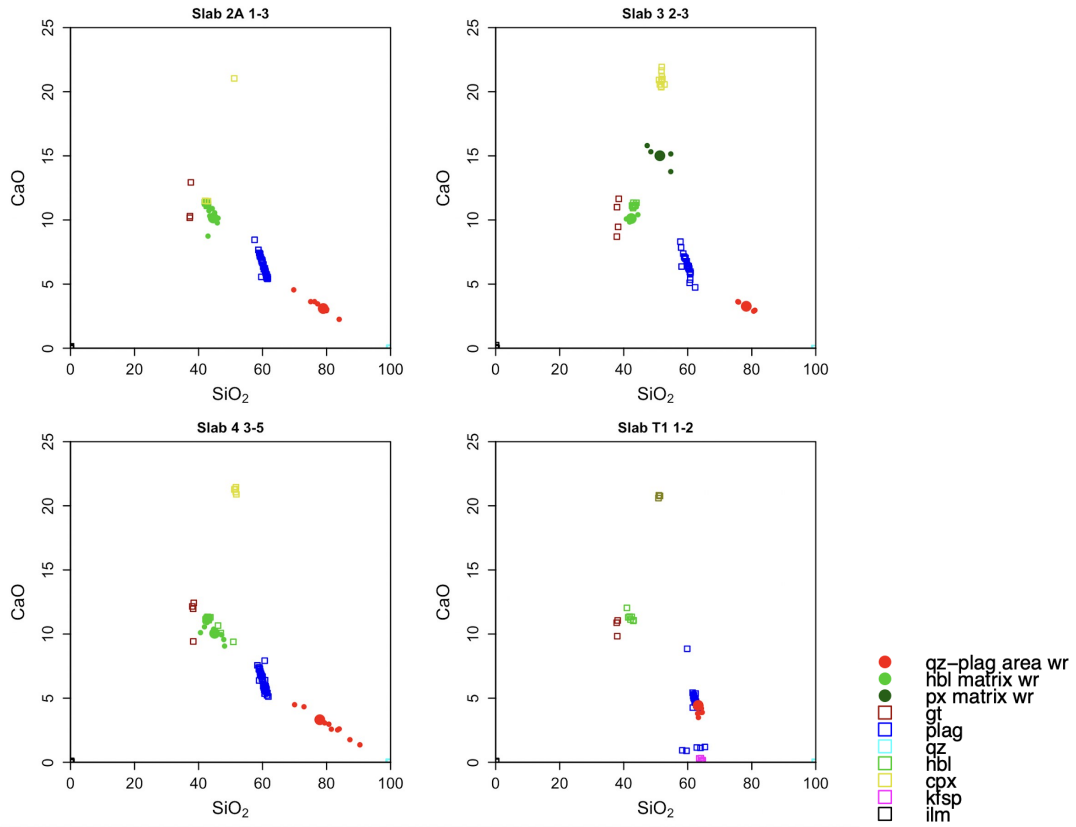

Appendix XI. Harker diagram with SiO_2 plotted against TiO_2, of the qz-plag area, matrix domains and the dominating minerals for the different sections. The mean values of the qz-plag areas and matrix domains are shown as larger dots. Plotted in GCDkit (Janousek et al., 2006). Abbreviations: wr: whole rock, hbl: hornblende, px: pyroxene, gt: garnet, plag: plagioclase, qz: quartz, cpx: clinopyroxene, kfsp: K-feldspar, ilm: ilmenite.

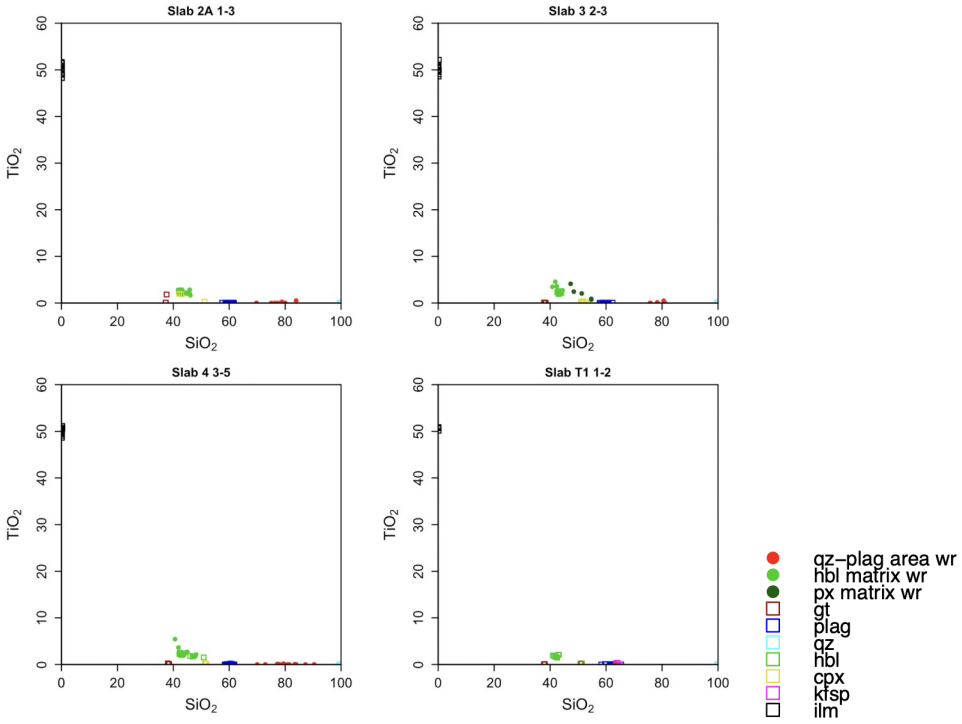

Appendix XII. EDS-analyses of 2000x2000 µm areas in the qz-plag areas of the garnet amphibolite and melt accumulation vein sample (section 2A (1/3), 3 (2/3), 4 (3/5) and T1 (1/2)).

qz-plag area wr																			
Section	2A (1/3)	2A (1/3)	2A (1/3)	2A (1/3)	2A (1/3)	2A (1/3)	2A (1/3)	2A (1/3)	3 (2/3)	3 (2/3)	3 (2/3)	3 (2/3)	4 (3/5)	4 (3/5)	4 (3/5)	4 (3/5)	4 (3/5)	4 (3/5)	4 (3/5)
Na2O	4.09	4.61	2.98	4.32	4.08	3.87	4.00	4.92	3.76	3.56	4.82	4.80	3.72	4.00	3.82	3.30	5.17	5.87	4.56
MgO	0.1	0.12	0.04	0.05	0.06	0.14	0.09	0.06	0.07	0.16	0.08	0.10	0.09	0.12	0.06	0.10	0.24	0.11	0.13
Al2O3	12.78	14.74	9.23	13.49	12.84	12.29	12.51	15.64	11.45	11.37	14.90	15.06	11.53	12.65	11.92	10.06	16.26	18.79	14.19
SiO2	79.26	76.25	83.94	78.31	78.8	80.06	79.96	75.03	80.59	81.00	75.89	75.66	81.48	79.39	80.71	83.45	72.94	70.01	77.19
P2O5	0.03	0	0.1	0	0.07	0.00	0.00	0.00	0.00	0.02	0.03	0.09	0.00	0.01	0.01	0.00	0.05	0	0.02
S	0	0	0	0.07	0.05	0.05	0.02	0.02	0.04	0.00	0.00	0.02	0.06	0.00	0.03	0.06	0.05	0.04	0
K2O	0.38	0.38	0.26	0.42	0.35	0.31	0.36	0.44	0.23	0.26	0.33	0.35	0.26	0.30	0.26	0.22	0.35	0.41	0.39
CaO	3.07	3.63	2.25	3.1	3.13	3.03	2.93	3.63	2.89	2.96	3.60	3.63	2.58	3.07	2.97	2.52	4.33	4.49	3.27
TiO2	0.01	0	0.53	0	0.25	0.00	0.01	0.00	0.49	0.05	0.00	0.00	0.00	0.17	0.00	0.05	0.01	0	0.1
V2O5	0	0.03	0	0	0.03	0.00	0.03	0.00	0.01	0.00	0.01	0.01	0.00	0.03	0.00	0.00	0	0.01	0.03
Cr2O3	0	0	0.01	0	0.03	0.00	0.00	0.04	0.00	0.00	0.01	0.01	0.00	0.00	0.00	0.03	0.01	0	0
MnO	0.02	0	0	0.06	0	0.01	0.00	0.00	0.01	0.00	0.04	0.00	0.00	0.01	0.00	0.00	0.07	0.05	0.01
FeO	0.24	0.24	0.67	0.17	0.31	0.25	0.11	0.21	0.42	0.63	0.29	0.27	0.22	0.24	0.21	0.21	0.52	0.17	0.11
ZrO2	0	0	0	0	0	0.00	0.00	0.00	0.03	0.00	0.00	0.00	0.05	0.00	0.02	0.00	0	0.06	0
Total	100	100	100	100	100	100	100	100	100	100	100	100	100	100	100	100	100	100	100
qz-plag area wr																			
Section	T1 (1/2)	T1 (1/2)	T1 (1/2)	T1 (1/2)	T1 (1/2)	T1 (1/2)	T1 (1/2)	T1 (1/2)	T1 (1/2	T1 (1/2	T1 (1/2	T1 (1/2	T1 (1/2	T1 (1/2	T1 (1/2	T1 (1/2	T1 (1/2	T1 (1/2	T1 (1/2
Na2O	8.08	7.85	8	8.1	8.2	7.99	8	7.95	8.06	7.98	7.82	7.97	8.22	8.09	8.39	8.16	8.28	8.87	7.92
MgO	0.13	0.18	0.09	0.1	0.06	0.1	0.09	0.1	0.08	0.08	0.08	0.13	0.11	0.14	0.15	0.06	0.06	0.14	0.16
Al2O3	23.1	22.75	23.45	23.24	23.58	23.4	23.12	22.61	23.11	22.9	22.42	23.37	23.69	22.44	23.08	23.32	23.18	22.86	22.1
SiO2	62.96	63.75	62.66	62.88	62.55	62.71	63.34	64.12	63.35	63.47	64.28	62.89	62.31	63.86	63.09	62.98	63.08	63.34	64.53
P2O5	0.05	0	0	0.03	0	0.01	0	0	0	0	0	0	0	0.01	0	0	0	0	0
S	0	0.01	0.02	0	0.01	0	0	0	0	0.04	0.04	0	0.02	0.04	0	0	0.02	0	0.1
K2O	0.61	0.63	0.54	0.61	0.56	0.64	0.8	0.95	0.61	0.68	0.86	0.64	0.55	0.83	0.99	0.76	0.84	0.93	0.88
CaO	4.66	4.55	4.96	4.73	4.85	4.86	4.37	3.89	4.59	4.62	4.2	4.77	4.79	4.35	3.8	4.45	4.31	3.49	3.89
TiO2	0.07	0	0.03	0.07	0.04	0	0.05	0.12	0.06	0	0.01	0.03	0.01	0.04	0.07	0.05	0	0	0.02
V2O5	0	0	0	0.01	0	0.06	0.01	0	0	0.01	0.02	0.04	0.05	0	0	0	0.04	0.08	0
Cr2O3	0.01	0	0	0.01	0.02	0.05	0	0	0	0	0	0	0.03	0.01	0.01	0.03	0	0	0.07
MnO	0.05	0	0.05	0.08	0.04	0	0	0.04	0.01	0.03	0.01	0	0	0	0	0	0	0	0
FeO	0.25	0.29	0.15	0.1	0.09	0.15	0.22	0.16	0.13	0.2	0.23	0.17	0.24	0.18	0.42	0.14	0.19	0.28	0.33
ZrO2	0.03	0	0.04	0.05	0	0.04	0	0.07	0	0	0	0	0	0.01	0	0.04	0	0	0
Total	100	100	100	100	100	100	100	100	100	100	100	100	100	100	100	100	100	100	100

Appendix XIII. EDS-analyses of 2000x2000 µm areas in the amphibolite matrix of the garnet amphibolite sample (section 2A (1/3), 3 (2/3) and 4 (3/5)).

hbl matrix wr																			
Section	2A (1/3)	2A (1/3)	2A (1/3)	2A (1/3)	2A (1/3)	2A (1/3)	2A (1/3)	2A (1/3)	3 (2/3)	3 (2/3)	3 (2/3)	4 (3/5)	4 (3/5)	4 (3/5)	4 (3/5)	4 (3/5)	4 (3/5)	4 (3/5)	4 (3/5)
Na2O	3.54	2.65	2.98	3.38	2.93	3.37	2.74	3.59	2.34	2.91	2.38	3.82	3.17	2.29	2.41	3.92	4.09	4.21	1.92
MgO	5.89	8.57	8.01	7.57	8.33	7.5	8.41	7.13	8.88	8.45	9.27	6.69	7.53	9.38	8.83	6.47	6.2	5.95	9.21
Al2O3	15.59	14.04	14.93	15.81	14.9	15.85	14.17	15.93	12.85	14.34	12.21	16.26	14.93	13.17	13.17	16.73	17.19	17.4	11.58
SiO2	42.95	43.24	44.29	45.77	45.03	46.1	43.48	45.86	40.82	44.43	41.84	47.88	44.71	42.68	41.85	47.06	47.24	48.13	40.61
P2O5	0.23	0.36	0.61	0.03	0.02	0.2	0.07	0.1	0.18	0.14	0.02	0.06	0.48	0.17	0.37	0.28	0.85	0.09	0.27
S	5.4	0.74	0.09	0.21	0.1	0.44	1.94	0.07	2.53	0.04	0.28	0.05	0.17	0.38	0.31	0.24	0.34	0.06	0.14
K2O	0.77	1.11	1.11	1.07	1.11	0.99	1.09	0.92	1.11	1.02	1.03	0.92	1.02	1.1	1.09	0.88	0.87	0.76	1.05
CaO	8.74	10.72	10.89	10.13	10.56	10.14	10.31	9.77	10.08	10.41	9.84	9.57	10.38	10.9	10.56	9.96	9.93	9.06	10.11
TiO2	2.36	2.47	2.05	2.14	2.04	1.66	1.98	2.84	3.47	2.72	4.54	1.74	2.57	2.53	3.64	1.88	1.59	2.16	5.44
V2O5	0.13	0.09	0.11	0.11	0.08	0.14	0.16	0.09	0.06	0.13	0.21	0.1	0.11	0.16	0.14	0.03	0.01	0.15	0.24
Cr2O3	0	0.04	0	0	0.03	0.01	0.01	0.05	0.02	0.03	0.06	0	0	0	0	0.1	0.08	0	0
MnO	0	0.06	0	0	0.04	0.05	0.02	0	0.06	0	0.11	0.04	0	0	0.08	0.01	0.02	0.1	0.05
FeO	14.37	15.83	14.88	13.78	14.77	13.49	15.56	13.57	17.59	15.36	18.21	12.87	14.92	17.24	17.46	12.34	11.58	11.91	19.39
ZrO2	0.03	0.09	0.04	0	0.05	0.06	0.07	0.07	0	0	0.01	0	0	0	0.08	0.09	0.02	0.01	0
Total	100	100	100	100	100	100	100	100	100	100	100	100	100	100	100	100	100	100	100

px matrix wr				
Section	3 (2/3)	3 (2/3)	3 (2/3)	3 (2/3)
Na2O	2.22	1.93	1.94	2.5
MgO	8.53	9.38	8.07	7.96
Al2O3	7.32	7.75	7.91	8.1
SiO2	47.33	48.47	54.69	54.7
P2O5	0.94	0.12	0.11	0
S	0.19	0.08	0.26	0.14
K2O	0.18	0.37	0.36	0.19
CaO	15.8	15.32	13.77	15.15
TiO2	4.11	2.43	0.73	0.89
V2O5	0.18	0.13	0.13	0.04
Cr2O3	0	0.13	0	0
MnO	0.06	0.14	0.01	0.12
FeO	13.05	13.75	12.01	10.12
ZrO2	0.09	0	0.01	0.09
Total	100	100	100	100

Tidigare skrifter i serien ”Examensarbeten i Geologi vid Lunds universitet”:

682. Rey, August, 2024: Isrörelser och havstransgressioner speglade Kåsebergåsen. (15 hp)
683. von Vultée, Anton, 2024: Babets kvarle vor - En morfologisk och sedimentologisk undersökning av överspolningssediment vid Tobisvik, Simrishamn. (15 hp)
684. Olsson Roso, Céline, 2024: Fåglarnas ursprung och tidiga utveckling. (15 hp)
685. Nawrocki, Bartosz, 2024: Karaktärisering av Cr-spinell i den ordoviciska Loka formationen vid Skultorps stenbrott, Billingen. (15 hp)
686. Rydh, Alexander, 2024: Unraveling Mag netic Anomalies: A Study of Earth's Field Asymmetries during the Laschamps Ex cursion. (15 hp)
687. Svensson, Ludvig, 2024: Echoes of im pact: A petrographic analysis and classifi cation of impact breccias from Hummeln, Sweden. (15 hp)
688. Pålsson, Malin, 2024: Detektion av utsläppsplymer med avancerat ekolod – Undersökning av utsläpp av avloppsvat ten från pappersbruk i havet med EK80, CTD & filmmaterial. (15hp)
689. Ivanovic, Edwin, 2024: Går det att se echinodermernas utveckling och diversifi ering under ordovicium i tunnslip? (15 hp)
690. Blomvall, Marlene, 2024: Analys av mor fologi, beteende och tafonomi hos ett ex ceptionellt bevarat fågelfossil från Furfor mationen (eocen), Danmark . (15 hp)
691. Elfström, Dari, 2024; Geomorfologisk studie av Jezerokraterns kant (Mars): Po tentiella mekanismer bakom kraterkan tens nuvarande utseende. (15 hp)
692. Andersson, Jacob, 2024: The Cerithium limestone Member at Stevns Klint reflect ing the carbonate production recovery after the K/Pg mass-extinction. (45 hp)
693. Adler, Linus, 2024: Petrografisk pilot studie av en högmetamorf epidotrik ber gart från Harbak, västra gnejsregionen i Norge. (15 hp)
694. Fält, Smilla, 2024: Dateringsmetoder för terrestriska nedslagskratrar med fokus på Siljan. (15 hp)
695. Kowal Johnson, Gloria, 2024: Traces of industrialization in a Baltic Sea sediment core with particular emphasis on marine traffic in Bornholmsgattet. (15 hp)
696. Riad, Musa, 2024: Bergkross som filter medium i artificiell infiltration. (15 hp)
697. Gleisner, Lovisa, 2024: Unravelling pri mary δ18O signatures of the 1730-36 Ti manfaya parental magmas on Lanzarote. (45 hp)
698. Johansson, Robin, 2024: Instrumentation of multilevel systems with transducers to characterize hydrogeological conditions at a PCE and TCE contaminated site in Helsingborg, Sweden. (45 hp)
699. Neumann, Daniel, 2025: Hydrogeological Dynamics of the Dalköpinge River: Inve stigating the Dry Spell Anomaly in a Hyd rogeological Context. (45 hp)
700. Durdek, Madeleine, 2025: Risk for water shortage in Ystad municipality - An evaluation of aquifer vulnerability to hu man impact. (45 hp)
701. Bouhal, Farah, 2025: Evolution of calcar eous nannoplankton in the Late Triassic: Insights at Eiberg Basin (Austria). (45 hp)
702. Barreby, Linn, 2025: Petrographic Analy sis of the Loftarstone Resurge Deposit in the Lockne Impact Structure, Sweden. (45 hp)
703. Dyson, Sarah, 2025: Environmental change in the Late Weichselian on the Kullen Peninsula. (45 hp)
704. Kardakos, Nikolaos, 2025: Caprock and reservoir assessment for CO2 storage in Lower Palaeozoic Formations of the Bal tic Sea subsurface: Textural, structural and mineralogical characterization using X-ray Computed Tomography, geochem istry and microscopy. (45 hp)
705. Filbà i Serra, Laura, 2025: Weichselian ice dynamics in Jämtland: Lithostrati graphic study of the Köttsjön till deposits. (45 hp)
706. Bäckehag, Kristoffer, 2025: Petrografisk studie av pseudotachylitisk breccia från nedslagskratern Siljan. (15 hp)
707. Zellman, Oskar, 2025: Karaktärisering av laminerade marina sediment under ett globalt utdöende (silur, Gotland). (15 hp)
708. Jögi, Amanda, 2025: En partiell hjärnskål från Åsens krita och dess koppling till den svenska svanödlefaunan. (15hp)
709. Rasmusson, Isak, 2025: Behovet av geolo gisk kunskap inom utbildning och sam hälle: En översikt av geologiskt innehåll i gymnasiets ämnesplaner, antagningar till svenska högskole - och universitetsutbild ningar inom geovetenskap och arbets marknadens behov av personer med geo logisk kompetens. (15hp)
710. Brede, Anton, 2025: Integrating Geologi cal Models and Geophysics to Estimate Hydraulic Properties - Providing a Foun dation for Hydrogeophysics Research. (15 hp)
711. Zimmermann, Moa, 2025: Utdöda organ ismers diet: Karaktärisering av en verte bratkoprolit från Skånes krittid. (15hp)
712. Popa, Alexandra, 2025: Aqueous altera tion in Martian meteorite Northwest Afri ca 11013: An analysis of its extent and origin. (15 hp)
713. Jónsdóttir, Svava Kristin, 2025: Ground ing zone wedges in the Nyköping area, southeastern Sweden. (45hp)
714. Heim, Emelie, 2025: Den sen- och post glaciala landskapsutvecklingen i Tvååker, Halland.

(15 hp)

715. Schiemann, Erik, 2025: Pollen och mikrofossil i en borrkärna från nedslagsstrukturen Hummeln. (15 hp)
716. Blomberg, Hampus, 2025: Vegetationsut vecklingen i Halland och Tvååker: sam manställning av underlag till infor mationsskyltar vid Naturplats Tvååkers Mosse. (15 hp)
717. Östman, Adrian, 2025: En litteraturstudie om grundvattendata och modeller som möjliga verktyg inom mineralprospekter ing. (15 hp)
718. Belcher, Carl Nils, 2025: Systematiska felkällor i deklinationsdata från sedi mentära borrkärnor. (15 hp)
719. Raas, Valérie, 2025: Cosmogenic Radio nuclide Evidence for a Solar Particle Storm at 14,300 BP. (45 hp)
720. Bjarkadóttir, Anna Bríet, 2025: Barome try of Clinopyroxene in Xenoliths from the Anaga Region in Tenerife – Con straints on the Magmatic Plumbing Sys tem. (45 hp)
721. Grönberg, Joel, 2025: Kan vulkanismen på Kanarieöarna ha uppkommit till följd av en hetfläck?. (15 hp)
722. Cordes, Beatrix, 2025: A review of the contaminant situation of groundwater aquifers in Europe – A historical retro spective and future outlook. (45 hp)
723. Alkasser, Shefaa, 2025: En litteraturstudie om mantelplymhypotesens eventuella tillkortakommanden utifrån ett kanariskt perspektiv. (15 hp)
724. Grönberg, Joel, 2026: Optically stimulat ed luminescence in Scania: An investiga tion into its applicability of determining provenance of coastal deposits. (45 hp)
725. Langkjaer, Henrik, 2026: Esker formation during deglaciation of the Scandinavian Ice Sheet, northeast Skåne and Blekinge, Sweden. (45 hp)
726. Corshammar, Johannes, 2026: Petrologisk-petrografisk studie av ankaramitbergarter på Teneriffa. (15 hp)
727. Sonesson, Ville, 2026: BC koncentrationer i sjösediment: en jä mförelse mellan Kina, Schweiz och Fin land. (15 hp)
728. Schönherr, Lara, 2026: Structural and petrographic characterization of the Mien impact structure, Sweden. (45 hp)
729. Meret, Ellison, 2026: Characterization of storm-surge deposits: A multi-proxy ap proach along the northern Halland coast with implications for organic carbon stor age. (45hp)
730. Ólafsdóttir Arnholtz, Edda, 2026: Con straining Weichselian high relative sea level events in Basissletta, northeastern Spitsbergen. (45 hp)
731. Persson, Frida, 2026: Windows of Mars: Impact Craters Along the Martian Dichot omy as Markers for Planetary Evolution. (15 hp)
732. Frödin, Anna, 2026: Industriella utsläpp till Östersjön - En kartläggning av utsläpp och effekter från pappers- och massain dustrin. (15 hp)
733. Österberg, Agnes, 2026: Från sund till ljung: Falsterbonäsets uppkomst och his torisk skogsförekomst på Skanörs ljung. (15 hp)
734. Ründla, Karoliina, 2026: Utveckling av markanvändning och vegetation i Söderåsens Nationalpark från senare delen av jägarstenåldern till nutid. (15 hp)
735. Pålsson, Malin, 2026: A Changing Foraminiferal Landscape in the Öresund: Cataloguing the Potentially Invasive Nonionella sp. T1 and Assessing Deep Learning for Species Identification. (45 hp)
736. Magnell, Ylva, 2026: Intracrustal partial melting of garnet amphibolite from south western Sweden - a possible analogue for TTG formation. (15 hp)

LUNDS UNIVERSITET

Institutionen för miljö– och geovetenskap
Lunds universitet
Sölvegatan 12, 223 62 Lund